APPLIED SCIENCES AND ENGINEERING

Metabotissugenic citrate biomaterials orchestrate bone regeneration via citrate-mediated signaling pathways

Hui Xu[1]†, Xinyu Tan[2]†, Ethan Gerhard[1], Hao Zhang[3], Rohitraj Ray[1], Yuqi Wang[1], Sri-Rajasekhar Kothapalli[1], Elias B. Rizk[4], April D. Armstrong[5], Su Yan[1]*, Jian Yang[3,6,7]*

Bone regeneration requires coordinated anabolic and catabolic signaling, yet the interplay between mammalian target of rapamycin complex 1 (mTORC1) and adenosine monophosphate–activated protein kinase (AMPK) pathways remains unclear. This study reveals that citrate, glutamine, and magnesium synergistically activate both pathways via calcium/calmodulin-dependent protein kinase kinase 2 (CaMKK2)– and protein kinase B (Akt)–dependent signaling, bypassing the traditional adenosine monophosphate (AMP)/adenosine triphosphate (ATP) sensing mechanism. This dual activation supports sustained energy metabolism during osteogenesis and challenges the canonical antagonism between mTORC1 and AMPK. We developed CitraBoneQMg, a citrate-based biomaterial incorporating these components via one-pot synthesis. CitraBoneQMg provides sustained release, photoluminescent and photoacoustic imaging capabilities, and tunable mechanical properties. In vitro, it promotes osteogenesis by enhancing alkaline phosphatase (ALP) activity, osteogenic gene expression, and calcium deposition. In vivo, it accelerates bone regeneration in a rat calvarial defect model while promoting anti-inflammatory and neuroregenerative responses. We define this integrated effect as "metabotissugenesis," offering a metabolically optimized approach to orthopedic biomaterial design.

INTRODUCTION

Recently, metabolism-regulating biomaterials have emerged as a transformative strategy in orthopedic engineering by enabling targeted modulation of intracellular metabolism through interactions with the local microenvironment (*1*–*5*). While material cues have long been known to influence cell behavior, their direct impact on cellular metabolic and signaling pathways is only beginning to be elucidated. Effective bone regeneration relies on a coordinated balance between anabolic and catabolic metabolism: Anabolic pathways support energy-intensive processes such as proliferation, matrix production, and osteogenic differentiation, while catabolic pathways—including glycolysis, fatty acid oxidation, and the tricarboxylic acid (TCA) cycle—regenerate adenosine triphosphate (ATP) and supply metabolic intermediates to sustain these activities (*6*). This coordination is regulated in part by two key metabolic sensors: the mammalian target of rapamycin complex 1 (mTORC1), which promotes anabolic growth under nutrient-rich conditions, and adenosine monophosphate-activated protein kinase (AMPK), which is activated during energy stress to conserve ATP, often by suppressing mTORC1 activity (*7*–*9*). The traditionally antagonistic relationship between mTORC1 and AMPK presents a challenge in understanding how cells meet the high metabolic demands of osteogenesis, which requires the coordinated activation of both anabolic and catabolic processes. While mTORC1 has been shown to support biosynthetic activity and osteogenic differentiation and AMPK to promote ATP production and stabilize transcription factors such as runt-related transcription factor 2 (RUNX2), previous studies have examined these pathways independently (*10*–*12*). As a result, the potential for their simultaneous activation and functional cross-talk during osteogenesis remains largely unexplored. Although brief, minute-scale coactivation of mTORC1 and AMPK by amino acids has been observed in other cell types (*13*), the dynamic regulation of these pathways in the context of long-term osteogenic differentiation is still poorly understood.

In this study, we identify two groundbreaking findings that reshape our understanding of metabolic coordination during osteogenesis: (i) Concurrent activation of mTORC1 and AMPK pathways by citrate, glutamine, and magnesium—a previously unrecognized synergy—supports energy-demanding biosynthetic processes while preserving cellular energy homeostasis. This dual activation enhances mitochondrial ATP production and anabolic activity, driving osteogenic differentiation efficiently. (ii) AMPK activation during osteogenesis occurs through calcium/calmodulin-dependent protein kinase kinase 2 (CaMKK2), a calcium-dependent pathway, rather than the traditional adenosine monophosphate (AMP)/ATP sensing mechanism. This energy-independent activation of AMPK links calcium signaling, a key regulator in osteogenesis, to metabolic processes, enabling AMPK to function even in energy-replete states. This bypass of the AMP-dependent pathway ensures that AMPK and mTORC1 can operate simultaneously without antagonism, aligning metabolic activity with osteogenic differentiation cues.

Building on these insights, we developed CitraBoneQMg, a citrate-based biomaterial designed to leverage this dual pathway activation. By integrating citrate, glutamine, and magnesium—key nutrients essential for intracellular energy metabolism—CitraBoneQMg enhances mitochondrial ATP production, activates both mTORC1 and AMPK signaling pathways, and drives robust osteogenic differentiation in mesenchymal stem cells (MSCs). Synthesized through a simple one-pot reaction, the biomaterial delivers sustained bioactive molecule release and features photoluminescent and photoacoustic

[1]Department of Biomedical Engineering, The Pennsylvania State University, University Park, PA 16802, USA. [2]Department of Traumatic Surgery, Center for Orthopaedic Surgery, The Third Affiliated Hospital of Southern Medical University, Guangzhou, Guangdong, PR China. [3]Department of Materials Science and Engineering, Westlake University, Hangzhou, Zhejiang 310030, PR China. [4]Department of Neurosurgery, Dell Medical School, University of Texas at Austin, Austin, TX 78712, USA. [5]Department of Orthopedics and Rehabilitation College of Medicine, The Pennsylvania State University, Hershey, PA 17033, USA. [6]Research Center for Industries of the Future, Westlake University, Hangzhou, Zhejiang 310030, PR China. [7]Center for Bio-based Materials, Muyuan Laboratory, 110 Shangding Road, Zhengzhou, Henan Province 450016, PR China.
*Corresponding author. Email: yangjian07@westlake.edu.cn (J.Y.); szy196@psu.edu (S.Y.)
†These authors contributed equally to this work.

properties for potential clinical applications, such as intraoperative guidance, longitudinal tracking of biomaterial fate, and noninvasive assessment of therapeutic efficacy.

In summary, our findings challenged the traditional dichotomy between mTORC1 and AMPK and highlighted the critical role of CaMKK2 signaling pathway in integrating metabolic regulation during bone regeneration. This study paves the way for designing advanced metabolism-regulating biomaterials that optimize energy metabolism and relevant signaling pathways for enhanced bone repair, offering transformative potential for orthopedic applications (Fig. 1).

RESULT

Citrate, glutamine and magnesium synergistically promote osteogenic differentiation of hBM-MSCs

To investigate osteogenic effects in our study, we used human bone marrow–derived MSCs (hBM-MSCs), which are well recognized for their capacity to differentiate into osteoblasts and their pivotal role in natural bone formation. Meanwhile, BM-MSCs have been widely used in osteogenesis research due to their well-characterized properties and clinical relevance (*14*–*17*). Therefore, they serve as an ideal in vitro model for studying bone regeneration in our experimental framework.

In the examination of the osteogenic effects of glutamine, distinct trends were observed in its impact during both undifferentiated hBM-MSCs proliferation and osteogenic differentiation. Glutamine is essential for undifferentiated hBM-MSCs proliferation, as supplementation with 0.5 mM glutamine (physiological serum concentration) significantly increased hBM-MSCs proliferation compared to cells cultured without glutamine (0 mM) (fig. S1A). However, higher concentrations of glutamine (1 to 8 mM) did not further enhance cell proliferation. Proliferation began to decline at high glutamine concentrations (16 and 32 mM) by day 3. These findings suggest that while glutamine is necessary for undifferentiated hBM-MSCs proliferation, a physiological concentration of 0.5 mM is sufficient. Conversely, during osteogenic differentiation, higher glutamine concentrations above the physiological level stimulated alkaline phosphatase (ALP) activity by day 7, with a dose-dependent effect observed, peaking at 8 mM (Fig. 2A). Similar to its effect in undifferentiated hBM-MSCs proliferation,

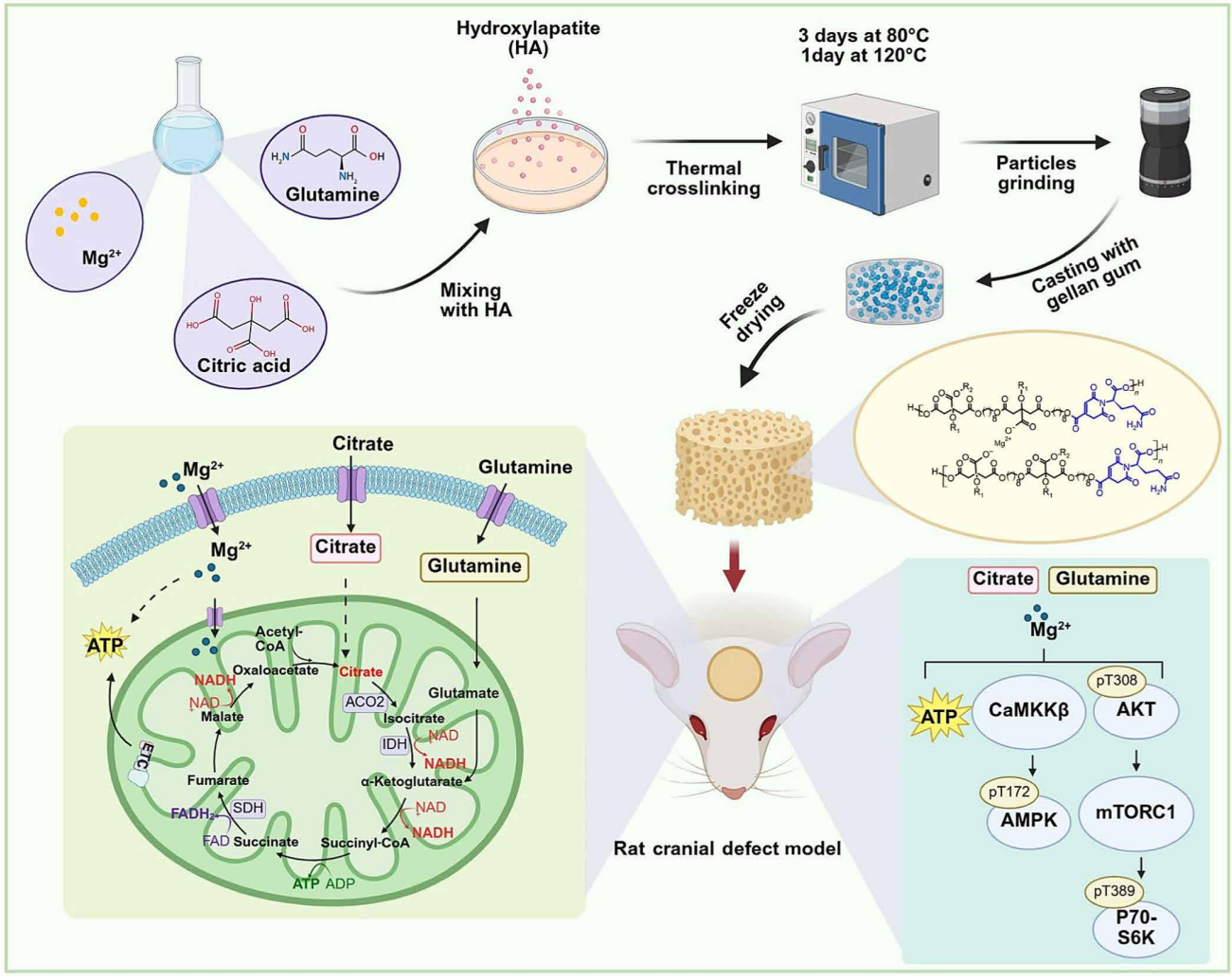

Fig. 1. Schematic illustration of composites fabrication procedures for bone regeneration with metabolic effect and involved signaling pathways. Figure created in BioRender [https://BioRender.com/tciloza; Hui Xu (2025)]. CaMMKβ, calcium/calmodulin-dependent protein kinase kinase β; mTORC1, mammalian target of rapamycin complex 1; AMPK, and adenosine monophosphate–activated protein kinase; ACO2, aconitase 2. ATP, adenosine triphosphate; NAD, nicotinamide adenine dinucleotide; NADH, reduced form of NAD^+; CoA, coenzyme A; IDH, isocitrate dehydrogenase; SDH, succinate dehydrogenase; FAD, flavin adenine dinucleotide; ADP, adenosine diphosphate.

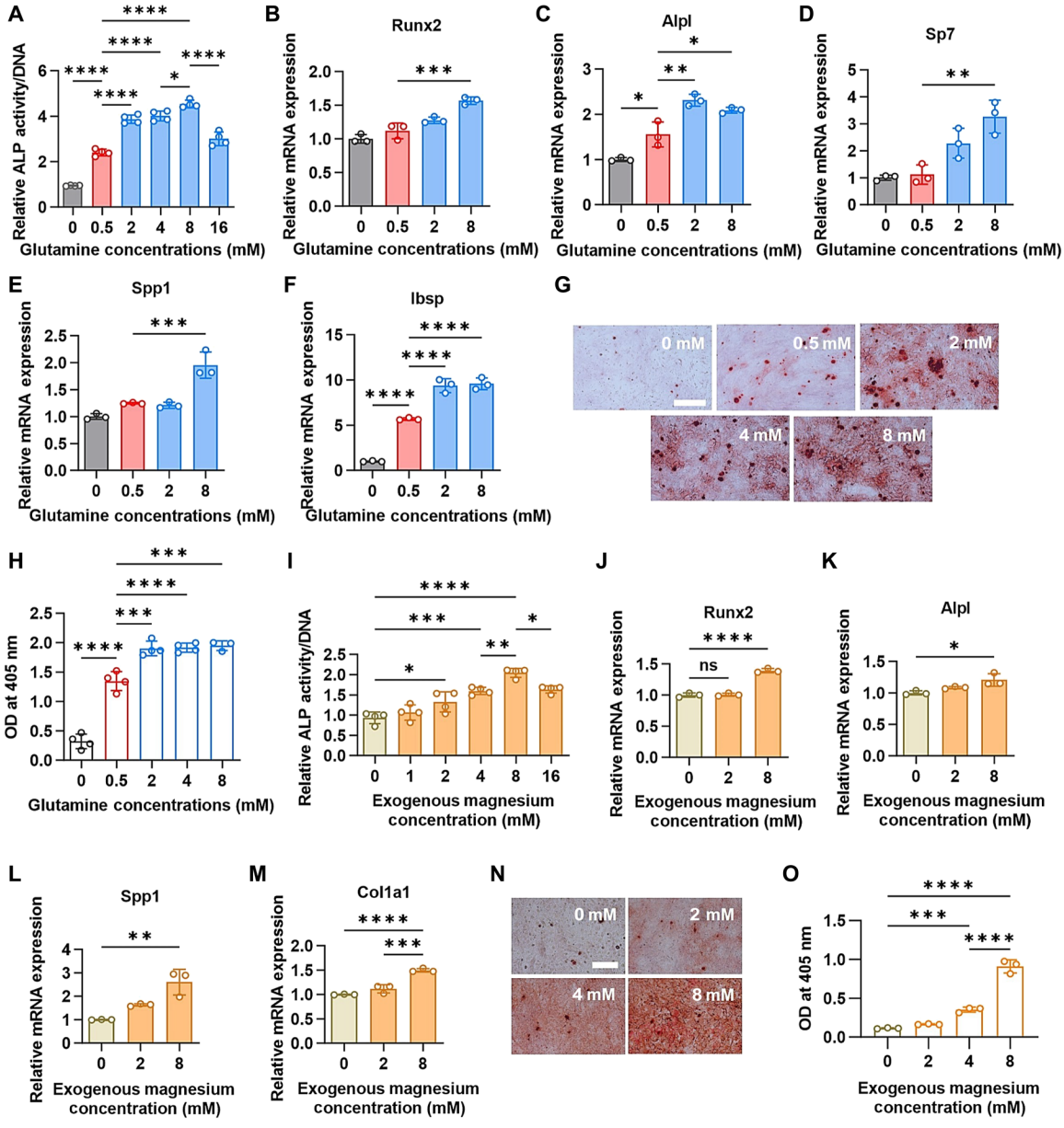

Fig. 2. Individual supplementation of glutamine and magnesium enhanced osteogenesis. (**A**) ALP activity on day 7 of osteogenic differentiation with various glutamine concentrations. Data are average ± SD. One-way ANOVA with Tukey's multiple comparisons test, *$P < 0.05$, **$P < 0.005$, ***$P < 0.0005$, and ****$P < 0.0001$. $n = 4$. (**B**) mRNA expression of Runx2 on day 4 of hBM-MSCs osteogenic differentiation with various glutamine concentrations. Data are average ± SD. One-way ANOVA with Tukey's multiple comparisons test, *$P < 0.05$, **$P < 0.005$, ***$P < 0.0005$, and ****$P < 0.0001$. $n = 3$. (**C** to **F**) mRNA expression of Alpl, Sp7, Spp1, and Ibsp on day 7 of hBM-MSCs osteogenic differentiation with various glutamine concentrations. Data are average ± SD. One-way ANOVA with Tukey's multiple comparisons test, *$P < 0.05$, **$P < 0.005$, ***$P < 0.0005$, and ****$P < 0.0001$. $n = 3$. (**G** and **H**) Representative images and quantification of calcium nodules deposition (red) with various glutamine concentrations on day 14 of hBM-MSCs osteogenic differentiation. Scale bar, 500 μm. Data are average ± SD. One-way ANOVA with Tukey's multiple comparisons test, *$P < 0.05$, **$P < 0.005$, ***$P < 0.0005$, and ****$P < 0.0001$. $n = 4$. (**I**) ALP activity on day 7 of osteogenic differentiation with various magnesium concentrations. Data are average ± SD. One-way ANOVA with Tukey's multiple comparisons test, *$P < 0.05$, **$P < 0.005$, ***$P < 0.0005$, ****$P < 0.0001$. $n = 4$. (**J**) mRNA expression of Runx2 on day 4 of hBM-MSCs osteogenic differentiation with various magnesium concentrations. (**K** to **M**) mRNA expression of Alpl, Spp1, and Col1a1 on day 7 of hBM-MSCs osteogenic differentiation with various magnesium concentrations. Data are average ± SD. One-way ANOVA with Tukey's multiple comparisons test, *$P < 0.05$, **$P < 0.005$, ***$P < 0.0005$, and ****$P < 0.0001$. $n = 3$. (**N** and **O**) Representative images and quantification of calcium nodules deposition (red) with various magnesium concentrations on day 14 of hBM-MSCs osteogenic differentiation. Scale bar, 500 μm. Data are average ± SD. One-way ANOVA with Tukey's multiple comparisons test, *$P < 0.05$, **$P < 0.005$, ***$P < 0.0005$, and ****$P < 0.0001$. $n = 3$. OD, optical density.

supplementation at 16 mM suppressed ALP activity. Furthermore, the expression of osteogenesis-related genes—including RUNX2, secreted phosphoprotein 1 (SPP1), Sp7 transcription factor (SP7), integrin-binding sialoprotein (IBSP), and ALP liver/bone/kidney (ALPL)—increased with higher glutamine concentrations compared to the 0.5 mM condition (Fig. 2, B to F). In addition, glutamine supplementation promoted calcium nodule deposition, a late marker of osteogenesis, by day 14 (Fig. 2, G and H). However, concentrations above 2 mM did not further enhance calcium nodule formation.

We also investigated the role of magnesium in undifferentiated hBM-MSC proliferation and osteogenic differentiation. The basal medium for hBM-MSCs contains 0.8 mM magnesium, the physiological serum concentration. Exogenous magnesium chloride ($MgCl_2$) supplementation at 1 mM began to promote undifferentiated hBM-MSC proliferation by day 5, exhibiting a dose-dependent effect (fig. S1B). As with glutamine, high magnesium concentrations (32 mM) led to decreased cell proliferation (fig. S1B). In terms of osteogenic differentiation, $MgCl_2$ supplementation similarly enhanced ALP activity, gene expression, and calcium nodule deposition up to 8 mM (Fig. 2, I to O), but excessive magnesium concentrations also suppressed ALP activity. These data suggest that physiological concentrations of glutamine (0.5 mM) and magnesium (0.8 mM) are not optimal for osteogenic differentiation, indicating that higher concentrations are beneficial.

Next, we explored whether combined supplementation of glutamine and Mg^{2+} could further enhance osteogenesis compared to individual treatments. Our results showed that varying $MgCl_2$ concentrations with 2 mM glutamine increased ALP activity (fig. S1C). Notably, higher $MgCl_2$ concentrations were necessary to enhance ALP activity as glutamine levels increased. These findings indicate that the simultaneous delivery of glutamine and magnesium could optimally support bone regeneration.

Our previous work demonstrated the osteopromotive effects of citrate, prompting us to investigate the combined effects of citrate, glutamine, and magnesium on osteogenesis. Based on previous findings, particularly those related to calcium nodule formation, we selected a combination of 2 mM glutamine, 8 mM magnesium, and 200 μM citrate for further experiments to assess their synergistic osteopromotive effects. Combining these three molecules significantly enhanced osteogenic differentiation in hBM-MSCs, as evidenced by increased ALP activity and gene expression (Fig. 3, A to C). We also see enhanced calcium nodule formation compared to citrate treatment only (Fig. 3, D and E). Fluorescence staining of ALP and osteopontin (OPN) on day 14 further confirmed that the combination of glutamine magnesium, and citrate elevates osteogenesis (Fig. 3, F to I). These exciting findings suggest that the concurrent supplementation of glutamine, magnesium, and citrate optimally promotes the osteogenic differentiation of hBM-MSCs.

Synergistic effect of citrate, glutamine, and magnesium on energy metabolism

Next, we investigated the mechanisms underlying the synergistic osteopromotive effects of glutamine, magnesium, and citrate. Osteogenic differentiation is an energy-demanding process, and all three compounds play distinct and essential roles in energy metabolism (*18*–*21*). Therefore, we assessed their effects on ATP production by measuring intracellular ATP levels during proliferation of undifferentiated hBM-MSCs and osteogenic differentiation, both individually and in combination.

During osteogenic differentiation, both glutamine and magnesium significantly elevated ATP levels at day 7 (Fig. 4, A and B) and exhibited a synergistic effect when combined with citrate at day 7 of osteogenesis (Fig. 4C). In contrast, no synergistic effect was observed during undifferentiated hBM-MSC proliferation (fig. S2). These results indicate that energy demand in undifferentiated hBM-MSCs is low; thus, energy metabolism maintains at a minimal level. Individual supplementation provides sufficient ATP for undifferentiated hBM-MSC proliferation. However, osteogenic differentiation requires more ATP; therefore, combined supplementation of citrate, glutamine, and magnesium provides the synergistic effect of producing higher ATP.

Most oxygen is used for ATP production during mitochondrial oxidative phosphorylation, making the oxygen consumption rate (OCR), a key indicator of energy metabolism. We used the Seahorse XFe instrument to measure dynamic changes in OCR during osteogenic differentiation with supplementation of citrate, glutamine, and magnesium (Fig. 4D). No significant differences were observed in non-mitochondria oxygen consumption and proton leak among the different treatment groups. Basal respiration, maximal respiration, and ATP production increased significantly in the citrate, glutamine, and magnesium combination treatment group compared to no treatment group (Fig. 4E). While these data suggested active mitochondrial activity, it was further confirmed by looking into mitochondria membrane potential. As shown in Fig. 4F, the mitochondria membrane potential increased after combined citrate, glutamine, and magnesium supplementation compared to citrate treatment alone. Together, these data indicate that combination of citrate, glutamine, and magnesium enhanced energy metabolism during osteogenesis, which in turn improved the osteogenic function.

Given the TCA cycle's crucial role in ATP production, we conducted metabolomic analyses to assess how glutamine, magnesium, and citrate influence the generation of TCA cycle metabolites on day 3 of osteogenic differentiation. Our results confirmed that most TCA cycle metabolites—including aconitate, α-ketoglutarate, succinate, fumarate, and malate—were elevated following supplementation (Fig. 4G and fig. S3). Notably, citrate/isocitrate, aconitate, α-ketoglutarate, succinate, and malate exhibited synergistic effects when citrate, glutamine, and magnesium were combined, indicating enhanced TCA cycle activity in the mitochondria. In addition, intracellular levels of citrate, glutamine, and magnesium were elevated after supplementation confirming the uptake of these molecules during osteogenic differentiation (fig. S4, A to C). The supplementation of citrate, glutamine, and magnesium increased global metabolism beyond the TCA cycle, including nucleotide and amino acid metabolism (Fig. 4H and fig. S5, A and B). These data suggest that citrate, glutamine, and magnesium enhanced overall energy production and global cellular metabolism to enhance osteogenesis.

Based on the osteogenic population in the hBM from single-cell RNA sequencing (scRNA-seq) dataset (GSE253355), we built a Uniform Manifold Approximation and Projection (UMAP) demonstrating the trajectory of osteogenesis process with different MSC-related cell types (fig. S6, A and B). Apolipoprotein D ($APOD^+$) MSC represents early stage, Osteo-MSC mid-stage, and osteoblast late-stage MSC osteogenic differentiation populations. Genes expressed in each cell type were analyzed to confirm the model's reliability. Accordingly, RUNX2 and IBSP were highly expressed in Osteo-MSCs and osteoblast, while THY and CD44 were enriched in $APOD^+$ MSCs (fig. S6C). In addition, the oxidative phosphorylation (OXPHOS)

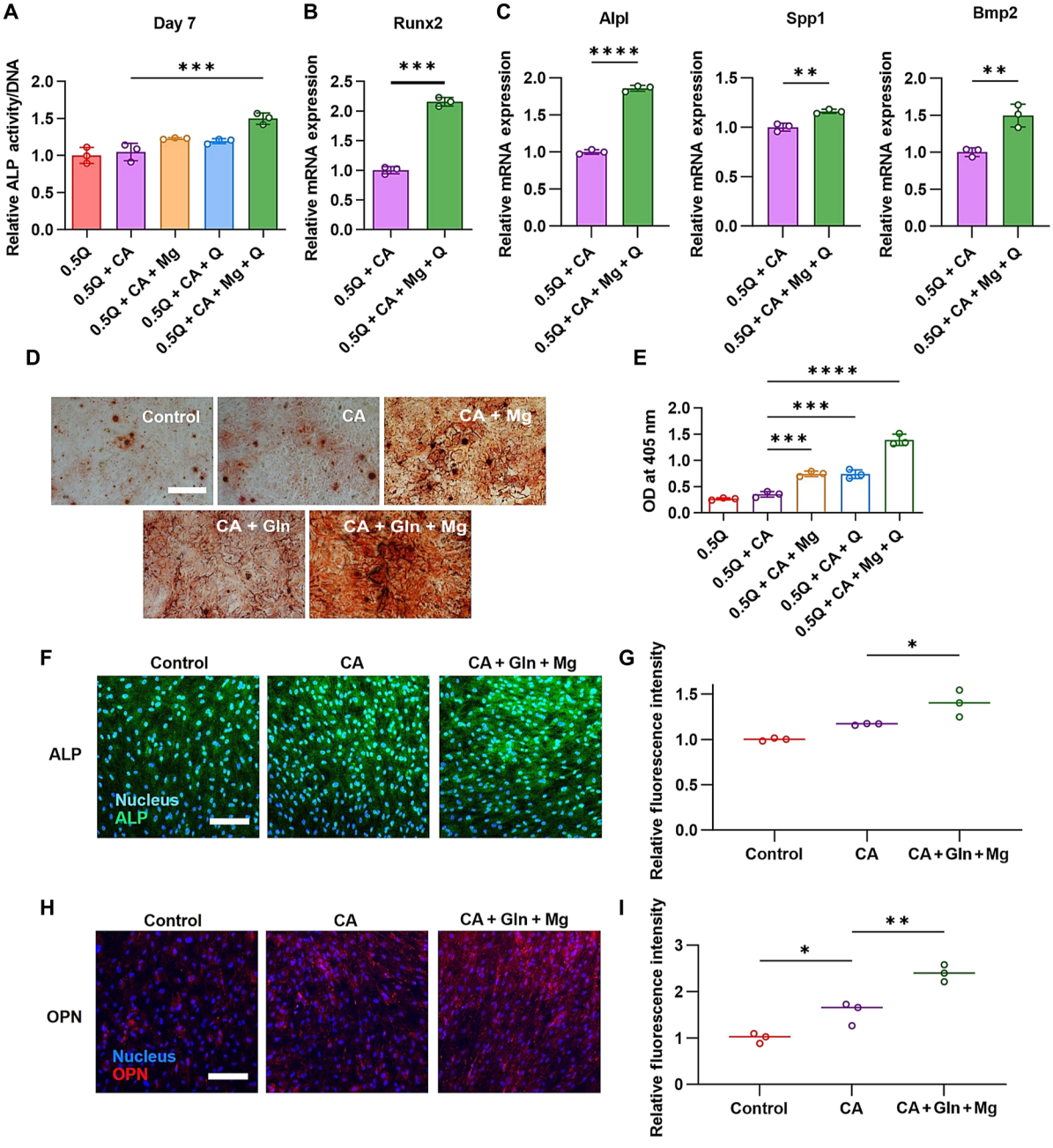

Fig. 3. Supplementation of citrate, glutamine, and magnesium synergistically enhanced osteogenesis. (**A**) ALP activity on day 7 of osteogenic differentiation with control, 200 μM citrate (CA), 200 μM citrate + 8 mM magnesium (CA + Mg), 200 μM citrate + 1.5 mM glutamine (CA + Gln), or 200 μM citrate + 1.5 mM glutamine + 8 mM magnesium (CA + Gln + Mg). Data are average ± SD. One-way ANOVA with Tukey's multiple comparisons test, *$P < 0.05$, **$P < 0.005$, ***$P < 0.0005$, and ****$P < 0.0001$. $n = 3$. (**B**) mRNA expression of Runx2 on day 4 of hBM-MSCs osteogenic differentiation with CA or CA + Gln + Mg. Data are average ± SD. Two-tailed unpaired *t* test, *$P < 0.05$, **$P < 0.005$, ***$P < 0.0005$, and ****$P < 0.0001$. $n = 3$. (**C**) mRNA expression of Spp1, ALPL, and BMP2 on day 7 of hBM-MSCs osteogenic differentiation with CA or CA + Gln + Mg. Data are average ± SD. Two-tailed unpaired *t* test, *$P < 0.05$, **$P < 0.005$, ***$P < 0.0005$, and ****$P < 0.0001$. $n = 3$. (**D** and **E**) Representative images and quantification of calcium nodules deposition (red) with control, CA, CA + Mg, CA + Gln, or CA + Gln + Mg on day 14 of hBM-MSCs osteogenic differentiation. Scale bar, 500 μm. Data are average ± SD. One-way ANOVA with Tukey's multiple comparisons test, *$P < 0.05$, **$P < 0.005$, ***$P < 0.0005$, and ****$P < 0.0001$. $n = 3$. (**F** and **G**) Representative images and quantification of ALP (green) immunofluorescence staining with DAPI nuclear counterstain (blue) on day 7 of hBM-MSCs osteogenic differentiation with control, CA or CA + Gln + Mg. Scale bar, 200 μm. (**H** and **I**) Representative images and quantification of OPN (red) immunofluorescence staining with DAPI nuclear counterstain (blue) on day 14 of hBM-MSCs osteogenic differentiation with control, CA, or CA + Gln + Mg. Scale bar, 200 μm. Data are average ± SD. One-way ANOVA with Tukey's multiple comparisons test, *$P < 0.05$, **$P < 0.005$, ***$P < 0.0005$, and ****$P < 0.0001$. $n = 3$. OPN, osteopontin.

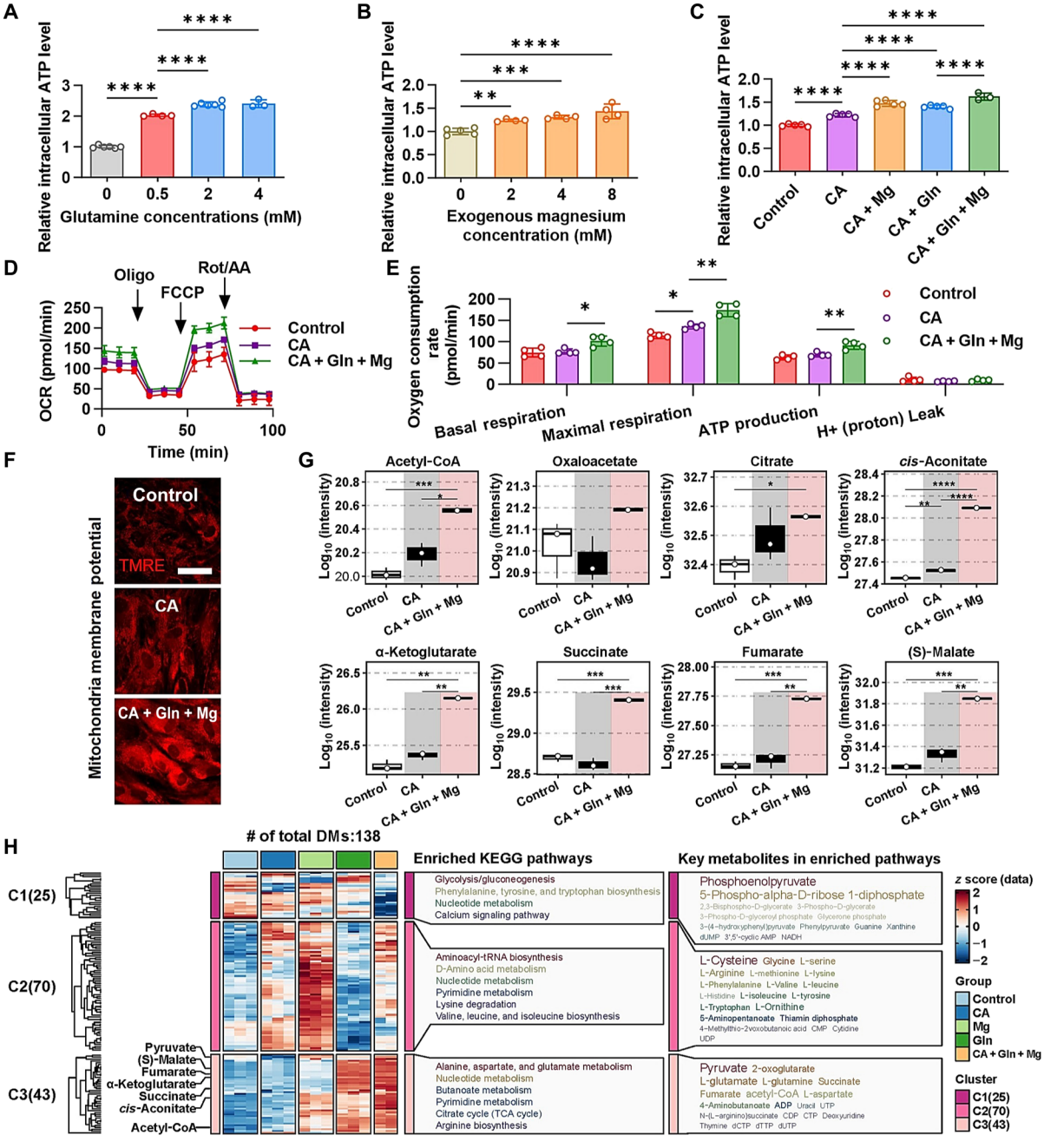

Fig. 4. Supplementation of citrate, glutamine, and magnesium synergistically enhanced energy metabolism. (**A**) Intracellular ATP level on day 7 of hBM-MSC osteogenic differentiation with various glutamine concentrations. Data are average ± SD. One-way ANOVA with Tukey's multiple comparisons test, *$P < 0.05$, **$P < 0.005$, ***$P < 0.0005$, and ****$P < 0.0001$. $n = 3$ to 6. (**B**) Intracellular ATP level on day 7 of hBM-MSC osteogenic differentiation with various magnesium concentrations. Data are average ± SD. One-way ANOVA with Tukey's multiple comparisons test, *$P < 0.05$, **$P < 0.005$, ***$P < 0.0005$, and ****$P < 0.0001$. $n = 4$. (**C**) Intracellular ATP level on day 7 of hBM-MSC osteogenic differentiation with control, CA, CA + Mg, CA + Gln, or CA + Gln + Mg. Data are average ± SD. One-way ANOVA with Tukey's multiple comparisons test, *$P < 0.05$, **$P < 0.005$, ***$P < 0.0005$, and ****$P < 0.0001$. $n = 3$ to 5. (**D**) OCR profile plot, (**E**) basal respiration, maximal respiration, ATP production, and proton leak at day 7 of hBM-MSCs ostegeogenic differentiation with control, CA, or CA + Gln + Mg. Data are average ± SD. One-way ANOVA with Tukey's multiple comparisons test, *$P < 0.05$, **$P < 0.005$, ***$P < 0.0005$, and ****$P < 0.0001$. $n = 4$. (**F**) Representative images of mitochondria membrane potential on day 7 of hBM-MSCs osteogenic differentiation with control, CA, or CA + Gln + Mg. Scale bar, 50 μm. (**G**) Intracellular levels of metabolites in TCA cycle on day 3 of hBM-MSCs osteogenic differentiation with control, CA, or CA + Gln + Mg. (**H**) Heatmap illustrating the intensity value distribution of 138 differential metabolites (DMs) across groups with CA, Gln, Mg, or CA + Gln + Mg. The significantly enriched KEGG pathways and their associated key metabolites from each cluster were displayed on the right side of the heatmap. Rot/AA, rotenone/antimycin A; FCCP, carbonyl cyanide *p*-trifluoromethoxyphenylhydrazone.

scores were increasing during the osteogenesis process approaching osteoblast (fig. S6D). Glutamine and magnesium transporters were highly expressed during osteogenesis, indicating the necessity of glutamine and magnesium for osteogenesis (fig. S6E).

Concurrent activation of mTORC1 and AMPK pathways

Because supplementation with citrate, glutamine, and magnesium has been shown to enhance intracellular ATP production, we further explored the energy metabolism-associated signaling pathways, including mTORC1 and AMPK. Traditionally, these two pathways have been perceived as antagonistic, where sufficient energy activates mTORC1, while energy deficiency activates AMPK (fig. S7A). However, previous studies have highlighted the important regulatory role of both (*22*, *23*). Our data also confirmed an overall up-regulation of both mTORC1 and AMPK activities during osteogenic differentiation of hBM-MSCs by demonstrating increased phosphorylation of p70-S6K, a downstream target of the mTORC1 pathway and a common indicator of mTORC1 activity, and enhanced AMPK phosphorylation (Fig. 5A), indicating the importance of mTORC1 and AMPK during osteogenic differentiation. Consistently, the inhibition of mTOR activity using rapamycin and Torin1 significantly decreased the osteogenic differentiation of hBM-MSCs, as evidenced by reduced ALP activities (fig. S7, B and C). The mTORC1 pathway integrates environmental signals, including amino acids and energy, to regulate cellular metabolism. Our prior research demonstrated that citrate enhances mTORC1-dependent protein synthesis in nondifferentiating hBM-MSCs (*24*). Here, we investigated the effect of citrate, glutamine, and magnesium on mTORC1 and AMPK signaling pathways during osteogenic differentiation.

As shown in Fig. 5B, individual supplementation with citrate, glutamine, and magnesium enhanced p70-S6K phosphorylation, indicating increased mTORC1 activity. In addition, we observed a synergistic effect of these three nutrients in further elevating mTORC1 signaling. Notably, this up-regulation was completely abolished upon treatment with Torin1, an mTOR inhibitor (Fig. 5C). While our in vitro cell studies (Fig. 4C) and metabolomics analysis (Fig. 5D) demonstrated that citrate, glutamine, and magnesium enhance intracellular energy production, we were surprised to find that their supplementation also led to increased AMPK phosphorylation (Fig. 5B).

The next question arises: Why is AMPK activated despite elevated intracellular ATP levels in osteogenic differentiating hBM-MSCs under our treatment conditions? In addition to the AMP/adenosine diphosphate (ADP)–dependent mechanism, CaMKK2 can also activate AMPK (*25*). To investigate the role of CaMKK2 in osteogenic differentiation, we applied STO-609, a specific inhibitor of CaMKK2, during differentiation. ALP activity significantly decreased with the addition of STO-609 (Fig. 5E). Western blot results confirmed that CaMKK2 inhibition reduced AMPK phosphorylation and abolished the effect of citrate, glutamine, and magnesium on increasing AMPK phosphorylation (Fig. 5F). These findings suggest that CaMKK2 positively regulates osteogenic differentiation and that its inhibition diminishes the osteogenic potential of hBM-MSCs.

The above findings raise the question of whether mTORC1 and AMPK communicate under nutrient-sufficient conditions during osteogenic differentiation. When STO-609, a CaMKK2 inhibitor, inhibited AMPK phosphorylation, p70-S6K phosphorylation increased (Fig. 5G). This suggests that AMPK and mTORC1 remain the traditional interconnected yet opposing relationship in OG differentiating hBM-MSCs. However, the up-regulation of mTORC1 activity by citrate, glutamine, and magnesium appears to override the antagonistic effect between AMPK and mTORC1, indicating that AMPK is not the dominant pathway regulating mTORC1 in this context.

Because AMPK is not the dominant upstream regulator of mTORC1, to explore the upstream signaling pathways that regulate mTORC1 activity, we examined the Akt pathway to explore the upstream signaling pathways that regulate mTORC1 activity. Akt stimulates mTORC1 activity by inhibiting tuberous sclerosis complex 1 and 2 (TSC1 and TSC2), which are negative regulators of mTORC1 activity (*26*). To determine whether citrate, glutamine, and magnesium activate mTORC1 via Akt, we used the allosteric Akt inhibitor MK-2206 with the three compounds. MK-2206 inhibited the phosphorylation of the mTORC1 substrate p70-S6K when combined with citrate, glutamine, and magnesium (Fig. 5H). In addition, the inhibition of Akt abolished the synergy effect of citrate, glutamine, and magnesium on ALP elevation (Fig. 5I). Furthermore, the supplementation of citrate, glutamine, and magnesium indeed increased phosphorylation of Akt at T308 (Fig. 5J). Western blot results also demonstrated the increase of phosphorylation of Akt over the osteogenic process of hBM-MSCs (Fig. 5A). Consistently, core genes in the AMPK pathway (PRKAA1), AKT pathway (AKT1), and mTOR pathway (MTOR, RPTOR, and RPS8KB1) were all highly expressed during osteogenesis in the model previously built using hBM scRNA-seq dataset (Fig. 5K). These results indicate that Akt indeed plays a vital role in osteogenesis and mediate the signaling from citrate, glutamine, and magnesium to mTORC1.

Calcium (Ca^{2+}) binding to calmodulin (CaM) is required for CaMKK2 activation. Therefore, we examined the effect of our three compounds on intracellular Ca^{2+} levels during osteogenic differentiation. Citrate, glutamine, and magnesium supplementation elevated intracellular Ca^{2+} levels at OG days 3 (fig. S7D). In addition, scRNA-seq dataset (GSE253355) analysis demonstrated the abundant gene expression of calcium-transporting channels throughout the osteogenesis process, suggesting the importance of calcium during osteogenesis (fig. S7E).

Together, these data indicate that citrate, glutamine, and magnesium concurrently up-regulate mTORC1 and AMPK signaling pathways during osteogenic differentiation. AKT and CaMKK2 serve as upstream regulators of mTORC1 and AMPK, respectively (Fig. 5L).

Incorporation of citrate, glutamine and magnesium into citrate-based polymer system

The data presented above demonstrate the intriguing synergistic osteopromotive effects of citrate, glutamine, and magnesium, highlighting their potential in promoting bone regeneration when used together. While glutamine and magnesium can traditionally be supplemented through diet, oral intake often fails to elevate their circulating concentrations to the levels necessary for optimal bone repair. Consequently, integrating them into biodegradable materials offers a promising strategy for local delivery in a controlled time- and dose-dependent manner, particularly for tissue regeneration in bone repair.

Citrate-based polymers have gained substantial attention recently (*4*, *5*, *27*–*31*). Using citric acid as a multifunctional monomer provides free pendant carboxylic acid groups that enhance hydroxyapatite (HA) binding through calcium chelation, allowing for up to 65 wt % HA incorporation in the citrate-based composite. In addition, integrating HA into citrate materials improves the mechanical properties of the materials and plays essential roles in facilitating tissue regeneration (*32*–*34*).

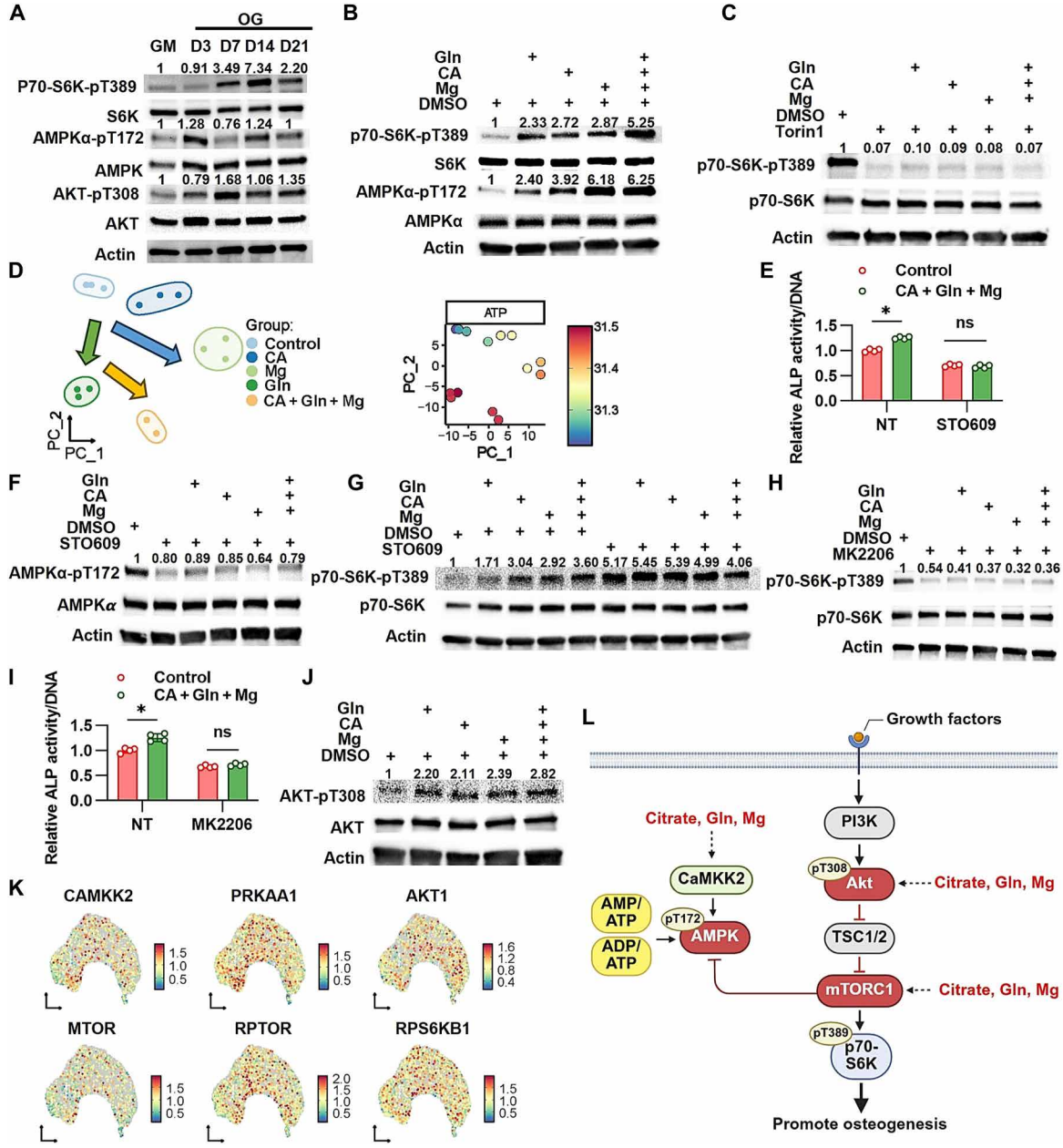

Fig. 5. Supplementation of citrate, glutamine, and magnesium activated energy-related signaling pathways. (**A**) Protein expression of p70-S6K-pT389, AMPKα-pT172, and AKT-pT308 at different days of hBM-MSCs osteogenic differentiation. (**B**) Protein expression of p70-S6K-pT389 and AMPKα-pT172 on day 3 of hBM-MSCs osteogenic differentiation with different treatments. (**C**) Protein expression of p70-S6K-pT389 on day 3 of hBM-MSCs osteogenic differentiation with Torin1 followed by different treatments. (**D**) Principal components analysis (PCA) of metabolomic data of hBM-MSCs osteogenic differentiation with different treatment conditions (left), and the intensity value distribution of ATP in the samples (right). The arrows denote the direction of three effects after different treatments. (**E**) ALP activity on day 7 of hBM-MSCs osteogenic differentiation without (NT) or with STO609 followed by without (control) or with CA + Gln + Mg treatment. Data are average ± SD. Two-tailed unpaired *t* test, $^{*}P < 0.05$, $^{**}P < 0.005$, $^{***}P < 0.0005$, and $^{****}P < 0.0001$. $n = 4$. (**F**) Protein expression of AMPKα-pT172 on day 3 of hBM-MSCs osteogenic differentiation with STO609, followed by different treatments. (**G**) Protein expression of p70-S6K-pT389 on day 3 of hBM-MSCs osteogenic differentiation with or without STO609, followed by different treatments. (**H**) Protein expression of p70-S6K-pT389 on day 3 of hBM-MSCs osteogenic differentiation with MK2206 followed by different treatments. (**I**) ALP activity on day 7 of hBM-MSCs osteogenic differentiation without (NT) or with MK2206 followed by without (control) or with CA + Gln + Mg treatment. Data are average ± SD. Two-tailed unpaired *t* test, $^{*}P < 0.05$. $n = 4$. n.s., not significant. (**J**) Protein expression of AKT-pT308 on day 3 of hBM-MSCs osteogenic differentiation with different treatments. (**K**) Expression of core genes in the CaMKK2 pathway (CaMKK2), AMPK pathway (PRKAA1), AKT pathway (AKT1), and mTOR pathway (MTOR, RPTOR, and RPS8KB1) within the human osteogenic population. (**L**) Schematic representation of the mTOR-AMPK network with citrate, glutamine, and magnesium supplementations. Figure created in BioRender [https://BioRender.com/a90y633; Hui Xu (2025)].

Furthermore, the combination of citrate chemistry with different diols results in a rich array of pendant carboxyl and hydroxyl groups, enabling the incorporation of various amino acids into the polymers to deliver essential nutrients. Our previous studies have shown that incorporating amino acids into citrate-based materials imparts fluorescence imaging properties, resulting in what we refer to as biodegradable photoluminescent polymers (BPLPs) (*28*, *35*–*38*).

To prepare BPLP-glutamine with or without magnesium (BPLP-Gln or BPLP-Gln-Mg), we conducted a one-pot condensation reaction involving citric acid, glutamine, and magnesium and 1,8-octanediol to create a prepolymer, which can then be polymerized to form an elastomeric cross-linked network (fig. S8, A and B). Multiple glutamine molar ratios were tested for prepolymer synthesis. On the basis of reaction efficiency, molar ratios of 0.3 and 0.5 were selected for further characterization. A 0.2 molar ratio for magnesium was initially chosen, according to previous studies in the laboratory involving divalent metal ion incorporation into citrate materials. The incorporation of glutamine and magnesium was confirmed through H–nuclear magnetic resonance (NMR) and Fourier transform infrared (FTIR) analysis (fig. S8, C to E), with poly(1,8-octanediol citrate) (POC) serving as a control. Energy dispersive x-ray spectroscopy (EDS) data further confirmed the integration of these three molecules and demonstrated their homogeneous distribution throughout the films (fig. S8F). Differential scanning calorimetry (DSC) and thermogravimetric analysis (TGA) were used to examine the thermal properties of the polymers. From DSC data, the glass transitioning temperature (T_g) was determined. Glutamine incorporation increased T_g due to the stiff ring structure formation after glutamine addition (fig. S8G). The addition of magnesium decreased T_g due to the potentially reduced cross-linking of the polymers as the complexation between Mg^{2+} and −OH/−COOH decreased the available −OH/−COOH for thermo-crosslinking (fig. S8, H and I). A similar trend was observed in TGA. The temperature required to reach 5% degradation increased as glutamine concentration increased (fig. S8J). Magnesium addition decreased the decomposition temperature (fig. S8, K and L).

However, the addition of glutamine compromises the compressive strength of the materials compared to POC. The active −OH and $-NH_2$ groups on glutamine compete with 1,8-octanediol for reaction with citric acid, weakening the network formation between 1,8-octanediol and citric acid, which subsequently decreases compressive strength. From POC to BPLP-0.3Gln, the compressive strength of the composites decreased from 260.85 ± 14.27 to 177.38 ± 17.64 MPa. As glutamine concentration increased, BPLP-0.5Gln composite showed a compressive strength of 144.49 ± 13.71 MPa. In contrast, incorporating magnesium helps restore compressive strength. BPLP-0.3Gln-Mg achieved an impressive compressive strength of 245.04 ± 26.12 MPa, which is comparable to POC (260.85 ± 14.27 MPa) (Fig. 6A).

To identify the optimal magnesium molar ratio, various magnesium concentrations were incorporated in BPLP-0.3Gln. The results demonstrated that BPLP-0.3Gln-0.2 Mg has the highest compressive stress and modulus (Fig. 6, B and C). Incorporation of magnesium did not affect the compressive strain of BPLP-0.3Gln (Fig. 6D). This increase in compressive strength is crucial for bone materials, as adequate mechanical stability is essential for load-bearing applications and long-term functionality in vivo. Thus, a 0.2 magnesium molar ratio was confirmed and applied to fabricate both BPLP-0.3Gln-Mg and BPLP-0.5Gln-Mg for further characterization. The modulus significantly decreased after glutamine incorporation (Fig. 6E). The compressive strain increased after glutamine incorporation from 47.15 ± 2.18% to 55.34 ± 2.64% to 60.41 ± 1.90% for POC, BPLP-0.3Gln, and BPLP-0.5Gln, respectively (Fig. 6F). Consistent with BPLP-0.3Gln, incorporation of magnesium increased the modulus of BPLP-0.5Gln and had minimum effect on compressive strain (Fig. 6, G and H).

By varying the amounts of glutamine incorporated, we can modulate the degradation rate of the materials. Increasing glutamine concentrations correlates with enhanced film degradation (Fig. 6I). BPLP-0.3Gln had ~40% weight remaining at week 24, whereas BPLP-0.5Gln was completely degraded. POC still had about 80% weight remaining at week 24. BPLP-0.3GLn-0.2 Mg degraded faster compared to BPLP-0.3Gln, where it had about 20% weight remaining. A similar trend was also observed in the pair of BPLP-0.5Gln and BPLP-0.5Gln-Mg. These findings suggest that by manipulating the polymer composition, we can effectively tailor mechanical properties and degradation rates, providing flexibility in the design of biomaterials to meet specific application requirements.

Imaging properties of BPLP-Gln and BPLP-Gln-Mg

Both BPLP-Gln and BPLP-Gln-Mg films emit fluorescence (fig. S9A). For BPLP-Gln films, fluorescence intensity decreases as molar ratio of glutamine increases (Fig. 6J). The addition of magnesium leads to decrease of fluorescence intensity (Fig. 6K). As shown in Fig. 6 (L to O), both BPLP-Gln and BPLP-Gln-Mg displayed excitation-dependent fluorescence emissions from 310 to 700 nm. The maximum emission and the excitation of both BPLP-0.3Gln and BPLP-0.5Gln are 440 and 340 nm, respectively (Fig. 6, L and M). The maximum emission and excitation wavelengths for BPLP-0.3Gln-Mg are 450 and 370 nm, respectively, where the maximum emission and excitation of BPLP-0.5Gln-Mg are 460 and 370 nm, respectively (Fig. 6, N and O). In addition, BPLP-Gln and BPLP-Gln-Mg demonstrated similar or better photostability than organic dyes, rhodamine B and fluorescein (fig. S9B), a key feature for many bioimaging applications. In addition, the incorporation of glutamine introduces photoacoustic property to the material across multiple wavelengths. A representative photoacoustic image at an 808-nm wavelength with a corresponding ultrasound image of the samples is shown in Fig. 6P. BPLP-0.5Gln film exhibits higher signal intensity than the BPLP-0.3Gln film (Fig. 6Q). In contrast, the addition of magnesium had no significant effect on photoacoustic signaling. With photoacoustic properties, our biomaterials can potentially enhance bioimaging diagnostics by enabling deeper tissue penetration, higher resolution, and improved contrast.

In vitro biocompatibility and bioactivity evaluation

Next, we examine whether the combination of citrate, glutamine, and magnesium can be successfully translated into a biomimetic material for orthopedic applications, here, we evaluate the biological activity of the material in vitro. First, high-performance liquid chromatography (HPLC) analysis of material releasing products in phosphate-buffered saline (PBS) buffer demonstrated the release of citrate, glutamine, and magnesium from the BPLP-Gln-Mg films (Fig. 7, A to C). An initial burst release of citrate, glutamine, and magnesium was observed in both BPLP-0.3Gln-Mg and BPLP-0.5Gln-Mg. Following the burst release, both the formulations could stably release citrate, glutamine, and magnesium at working concentrations. Next, both leachant and degradation products of the materials were evaluated with L929 cells for testing the biocompatibility of the polymers

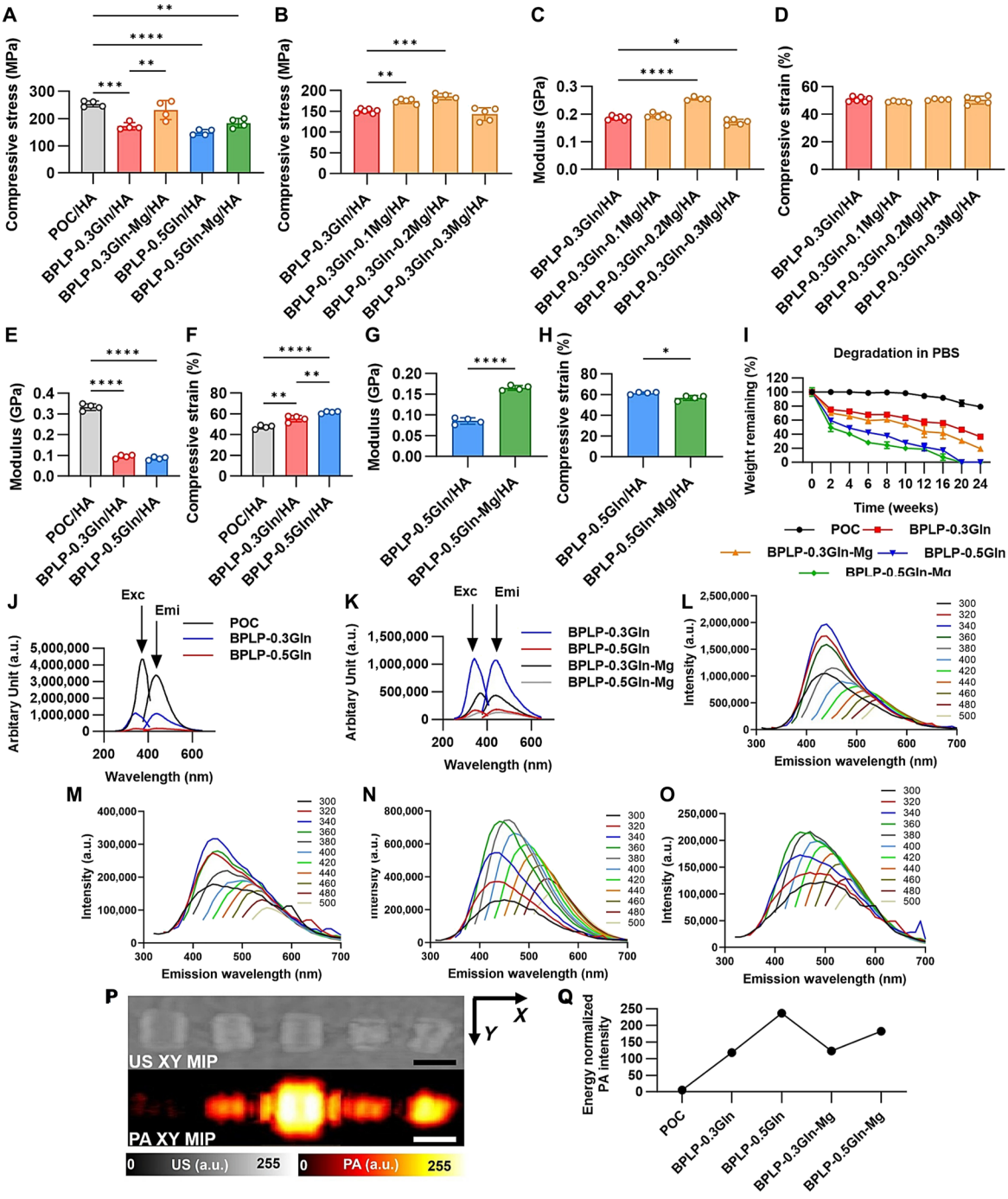

Fig. 6. Material characterization of BPLP-Gln-Mg. (**A**) Compressive stress of POC, BPLP-0.3Gln, BPLP-0.3Gln-Mg, BPLP-0.5Gln, and BPLP-0.5Gln-Mg composites. Data are average ± SD. One-way ANOVA with Tukey's multiple comparisons test, $^{*}P < 0.05$, $^{**}P < 0.005$, $^{***}P < 0.0005$, and $^{****}P < 0.0001$. $n = 4$. (**B**) Compressive stress, (**C**) modulus, and (**D**) compressive strain of composites with incorporation of various magnesium amounts. Data are average ± SD. One-way ANOVA with Tukey's multiple comparisons test, $^{*}P < 0.05$, $^{**}P < 0.005$, $^{***}P < 0.0005$, and $^{****}P < 0.0001$. $n = 4$ to 6. (**E**) Modulus and (**F**) compressive strain of POC and BPLP composites with incorporation of various glutamine amounts. Data are average ± SD. One-way ANOVA with Tukey's multiple comparisons test. $^{*}P < 0.05$, $^{**}P < 0.005$, $^{***}P < 0.0005$, and $^{****}P < 0.0001$, $n = 4$. (**G**) Modulus and (**H**) compressive strain of BPLP-0.5Gln with or without magnesium incorporation. Data are average ± SD. Two-tailed unpaired *t* test, $^{*}P < 0.05$, $^{**}P < 0.005$, $^{***}P < 0.0005$, and $^{****}P < 0.0001$. $n = 4$. (**I**) Degradation of POC, BPLP-0.3Gln, BPLP-0.3Gln-Mg, BPLP-0.5Gln, and BPLP-0.5Gln-Mg films in PBS over time. $n = 3$. (**J**) Excitation and emission of POC film and BPLP films with various glutamine amounts. (**K**) Excitation and emission of BPLP-0.3Gln film and BPLP-0.5Gln films with magnesium incorporation. (**L**) Emission spectra of BPLP-0.3Gln film. (**M**) Emission spectra of BPLP-0.3Gln-Mg film. (**N**) Emission spectra of BPLP-0.5Gln film. (**O**) Emission spectra of BPLP-0.5Gln-Mg film. (**P**) Ultrasound (US) image (above) and 3D photoacoustic (PA) image (below) of POC, BPLP-0.3Gln, BPLP-0.5Gln, BPLP-0.3Gln-Mg, and BPLP-0.5Gln-Mg films from left to right at 808-nm wavelength. Scale bars, 3 mm. (**Q**) Quantitative analysis of the 3D photoacoustic image at 808-nm wavelength. a.u., arbitrary unit.

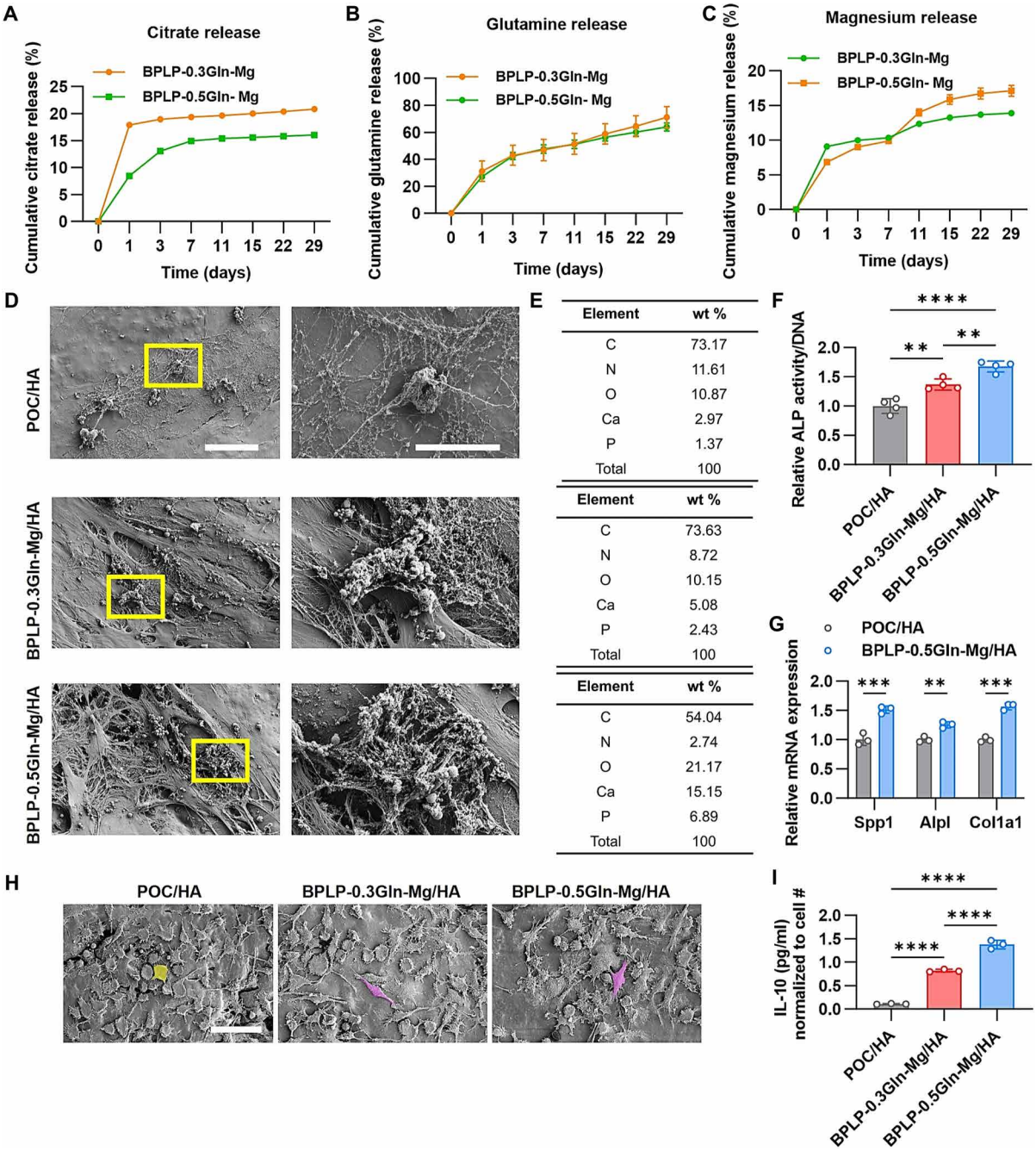

Fig. 7. In vitro bioactivity evaluation of BPLP-Gln-Mg materials. (**A** to **C**) Release of citrate, glutamine, and magnesium from BPLP-0.3Gln-Mg and BPLP-0.5Gln-Mg films over time. $n = 3$. (**D**) SEM images and EDS analysis of calcium nodule formation on day 21 of hBM-MSCs osteogenic differentiation on various composites. Right images are zoom-in of the yellow rectangles on the left accordingly. Scale bars, 50 μm (left) and 20 μm (right). (**E**) EDS quantification of corresponding composites on day 21 of hBM-MSCs osteogenic differentiation. (**F**) ALP activity on day 7 of hBM-MSCs osteogenic differentiation on various composites. Data are average ± SD. One-way ANOVA with Tukey's multiple comparisons test, $^{*}P < 0.05$, $^{**}P < 0.005$, $^{***}P < 0.0005$, $^{****}P < 0.0001$. $n = 4$. (**G**) Osteogenic mRNA expression of Spp1, Alpl, and Col1a1 on day 7 in hBM-MSCs undergoing osteogenic differentiation on various composites. Data are average ± SD. Two-tailed unpaired *t* test, $^{*}P < 0.05$, $^{**}P < 0.005$, $^{***}P < 0.0005$, $^{****}P < 0.0001$, $n = 3$. (**H**) SEM images of Raw 264.7 cells on POC, BPLP-0.3Gln-Mg and BPLP-0.5Gln-Mg composites. Scale bar, 50 μm. Representative M1 and M2 morphology is highlighted in yellow and magenta, respectively. (**I**) IL-10 release of Raw 264.7 cells grown for 3 days on POC, BPLP-0.3Gln-Mg and BPLP-0.5Gln-Mg composites. Data are average ± SD. One-way ANOVA with Tukey's multiple comparisons test, $^{**}P < 0.005$, $^{***}P < 0.0005$, $^{****}P < 0.0001$. $n = 3$.

(fig. S10). POC, BPLP-0.3Gln-Mg, and BPLP-0.5Gln-Mg did not show any cytotoxicity after 10× dilution.

Osteogenic differentiation of hBM-MSCs was performed on BPLP-Gln-Mg/HA composite discs to access the osteogenic property of the polymer. Scanning electron microscopy (SEM) images demonstrated thicker layers of cells and extensive extracellular matrix production after incorporation of magnesium and glutamine compared to POC, where BPLP-0.5Gln-Mg/HA showed the best bioactivity (Fig. 7D). Calcium nodules formation was visualized in the image. The analysis of these nodules by EDS demonstrated comparable calcium to phosphate ratio to HA among three groups (Ca/P = 1.68, 1.62, and 1.70 for POC, BPLP-0.3Gln-Mg/HA, and BPLP-0.5Gln-Mg/HA composites, respectively) (Fig. 7E). Furthermore, the ALP production in BPLP-0.5Gln-Mg/HA is significantly higher than POC/HA on day 7 (Fig. 7F). Aligned with the mechanical testing results, SEM images and ALP production also demonstrated that 0.2 molar ratio of magnesium incorporation is optimal for bioactivity of the composites (fig. S11, A and B). In addition, BPLP-0.5Gln-Mg/HA exhibited significantly higher SPP1, ALPL, and COL1a1 gene expression than POC/HA (Fig. 7G). The results of biological evaluations prove that BPLP-0.5Gln-Mg/HA could create an interactively biomimetic matrix microenvironment, which promoted hBM-MSCs osteogenic differentiation.

Glutamine and magnesium are known for having anti-inflammatory properties (*39*–*41*). Raw 264.7 cells seeded on composites showed more M2-like morphology (spindle-like shape) on BPLP-Gln-Mg/HA composites compared to POC composite, where majority of cells showed M1-like morphology (pancake-like shape) (Fig. 7H). Consistently, our data also demonstrated that BPLP-0.3Gln-Mg/HA and BPLP-0.5Gln-Mg/HA composites induce higher release of interleukin-10 (IL-10), a well-known anti-inflammatory cytokine, compared to POC composite where BPLP-0.5Gln-Mg/HA showed superior result (Fig. 7I).

In vivo evaluation of BPLP-Gln-Mg for bone regeneration

Given the best osteogenic bioactivity of the BPLP-0.5Gln-0.2 Mg/HA composite in vitro, we implanted BPLP-0.5Gln-0.2 Mg/HA scaffolds into critical-sized calvarial bone defects in rats to further evaluate the bone regeneration efficacy of BPLP-0.5Gln-0.2 Mg/HA in vivo. For convenience, the material is referred to as BPLP-Gln-Mg/HA. Micro–computed tomography (CT), histological staining, and immunohistochemical staining were performed to assess the newly formed bone tissue within the defect area. Micro-CT was taken 6 and 12 weeks after scaffold implantation, and three-dimensional (3D) reconstructed micro-CT images of new bone formation in vivo of different groups are shown in Fig. 8A. Weeks 6 and 12 were chosen to assess both the early-to-mid phase and the long-term stability, structural integrity, and functional quality of the regenerated bone, respectively (*42*–*45*). The control group, poly(lactic-*co*-glycolic acid) (PLGA)/HA, showed delayed fracture healing and repair, indicating a larger defect area compared to the citrate-based scaffold groups. On the contrary, BPLP-Gln-Mg/HA scaffold showed the highest efficiency of bone repair, with significant bone production by the end of 6 weeks. By 12 weeks post-implantation, the bone defect of the BPLP-Gln-Mg/HA scaffold was almost filled with new bone. Quantitative analysis showed that the bone/tissue volume (BV/TV) ratio was significantly higher in the POC/HA (21.97 ± 2.52, 29.84 ± 3.09) group than in the control (10.11 ± 1.74, 16.46 ± 1.46) at both 6 and 12 weeks. At the same time, the highest percentage of BV/TV of new bone formation was found in the BPLP-Gln-Mg/HA scaffold (31.69 ± 6.39, 49.09 ± 9.39) compared to all other groups, indicating a better bone regeneration effect (Fig. 8, B and C). Similarly, the bone mineral density (BMD) in POC/HA group (667.78 ± 75.41, 1047.9 ± 9.09) was significantly higher compared to the control (456.46 ± 43.386, 811.67 ± 82.50) at both 6 and 12 weeks. Likewise, BMD in BPLP-Gln-Mg group (966.67 ± 14.53, 1147.20 ± 27.95) was significantly higher than all other groups (Fig. 8, D and E).

The ability of the BPLP-Gln-Mg/HA scaffold to mediate bone regeneration was further investigated by histological analysis including hematoxylin and eosin (H&E) staining and Masson's trichrome staining (Fig. 8F). By observing the H&E staining sections 6 and 12 weeks after implantation, only fibrous tissue was visible in the defect area with hardly any new bone formation at 6 weeks post-implantation in PLGA/HA group. In contrast, more regenerative bone tissue was formed in POC/HA group. Moreover, the BPLP-Gln-Mg/HA group had the greatest bone formation, and newly regenerated bone was observed even at the center of the defect. In addition, the bone defect was almost filled with newly regenerated bone 12 weeks after implantation. However, material residues from scaffold degradation were found in the defect areas even at 12 weeks post-implantation due to the incomplete degradation at this point of implantation. Meanwhile, Masson's trichrome staining confirmed that BPLP-Gln-Mg/HA scaffold induced the highest amounts of mature mineralized bone formation within the bone defect area at both time points.

In addition, immunohistochemical staining was performed at 6 and 12 weeks post-implantation to investigate possible osteogenic-related expression during the bone regeneration process (Fig. 9). Higher osteo-related expressions of RUNX2 and OCN in the BPLP-Gln-Mg/HA were confirmed. The BPLP-Gln-Mg/HA restored calvarial defect without exogenous growth factors/cells, enhancing its clinical translatability. Besides up-regulating signaling pathways and energy metabolism, implantable biomaterials with favorable immune responses also guide successful osteogenesis (*46*, *47*). Previous publications have already demonstrated that glutamine and magnesium have anti-inflammatory properties (*41*, *48*–*50*). Our IHC staining of CD206, an anti-inflammation marker, also revealed that BPLP-Gln-Mg expressed anti-inflammatory effect at week 6. POC/HA showed CD206 marker at week 12. However, PLGA/HA did not express any CD206 at either time point. This is consistent with our in vitro data, where BPLP-0.5Gln-Mg/HA induced a higher amount of IL-10 release from Raw 264.7 compared to POC, which contributed to bone regeneration in vivo (Fig. 7I). Besides bone formation, nerve regeneration also plays a crucial role in bone regeneration. Here, the first time, we revealed the promotive effect of POC on nerve regeneration in a rat calvarial defect model. TUBB3, a marker for nerve regeneration, was expressed at both week 6 and week 12 after implantation in POC/HA group. Notably, TUBB3 was largely expressed in BPLP-Gln-Mg/HA group at both week 6 and week 12 post-implantation. In contrast, TUBB3 in the PLGA/HA group was minimal at both weeks 6 and 12. In addition, the fluorescence properties of POC and BPLP-Gln-Mg aided in the degradation tracking in vivo. At week 12 post-implantation, POC/HA and BPLP-Gln-Mg/HA groups demonstrated higher fluorescence compared to PLGA/HA group (fig. S12). These results indicate that local delivery of citrate, glutamine, and magnesium greatly restored the structural integrity and promoted functional regeneration of calvarial bone tissue. We named the HA-incorporated BPLP-Gln-Mg bone material as CitraBoneQMg.

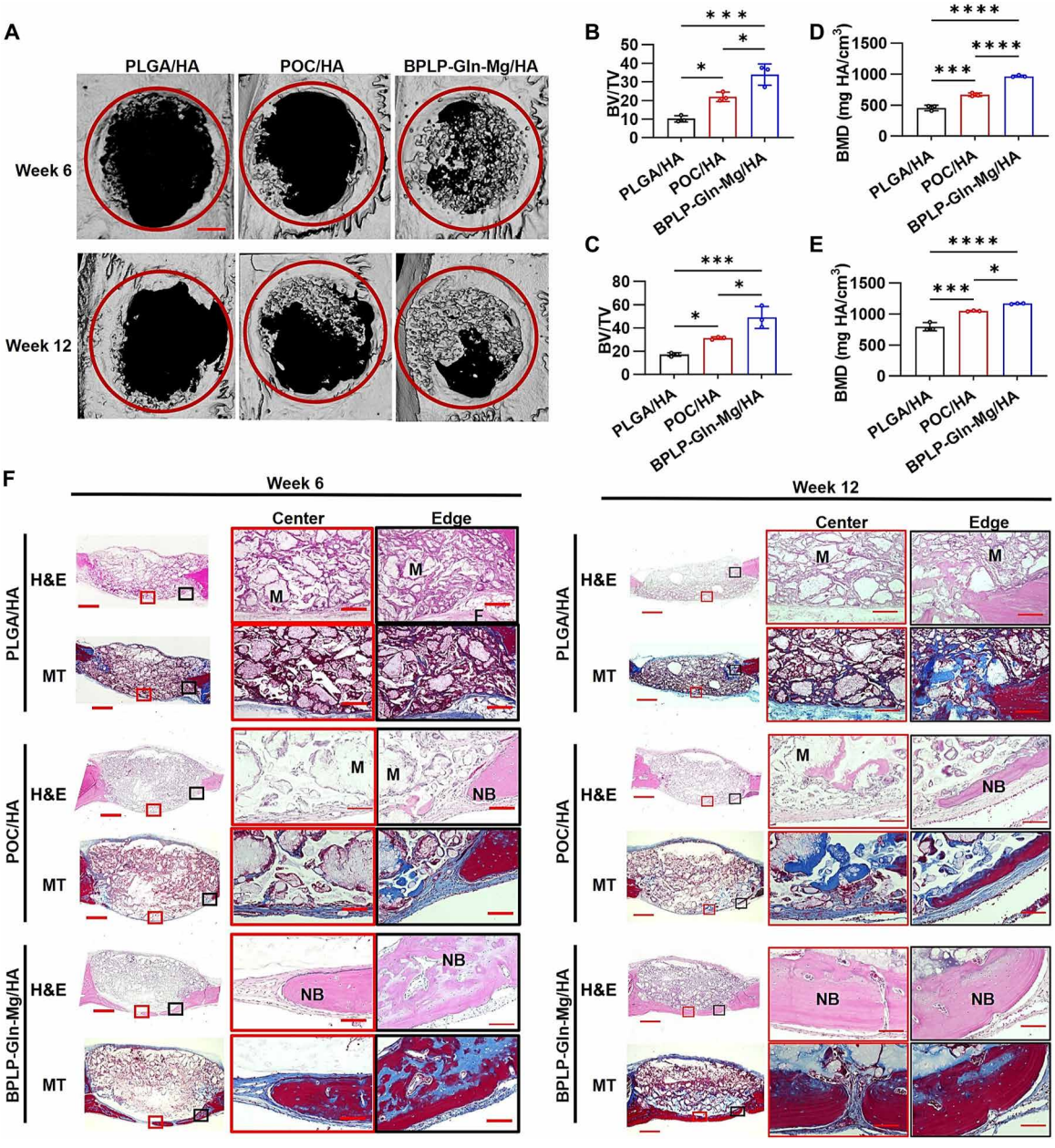

Fig. 8. In vivo new bone formation in a rat calvarial bone defect model. (**A**) Micro-CT images of calvaria defects with PLGA/HA, POC/HA, and BPLP-Gln-Mg/HA scaffolds at 6 and 12 weeks post-surgery. Scale bar, 1 mm. (**B** to **E**) Quantitative analysis of new bone formation at 6 (B and D) and 12 weeks (C and E). BV/TV, bone volume/tissue volume; BMD, bone marrow density. Data are average ± SD. One-way ANOVA with Tukey's multiple comparisons test, $*P < 0.05$, $***P < 0.0005$, $****P < 0.0001$. $n = 3$. (**F**) H&E and Masson's trichrome (MT) staining of calvaria bone samples at 6 and 12 weeks post-surgery. Scale bars, 1 mm (zoom out) and 50 μm (zoom in) (M, material; F, fibrosis tissue; NB, new bone).

DISCUSSION

Citrate, well known for its role in cellular metabolism, has emerged as a key regulator of broader cellular functions. By enhancing intracellular energy levels through mitochondrial pathways, citrate supports the increased metabolic demands of osteogenesis—establishing the foundation for its multifaceted role in tissue regeneration, a central feature of "metabonegenesis" (*24*). In this study, we further identify citrate as a signaling molecule that activates both the mTORC1 and AMPK pathways during osteogenic differentiation. The simultaneous activation of these typically antagonistic pathways underscores citrate's unique capacity to coordinate metabolic and signaling networks during bone formation.

Traditionally, AMPK activation inhibits mTORC1 under low-energy states, preventing excessive anabolic activity during energy scarcity (*51*). While a previous systems biology study demonstrated that amino acids can acutely and transiently activate both mTORC1 and AMPK in multiple cell lines, its findings were primarily limited to short-term signaling responses in vitro, without the evidence of sustained activation or functional outcomes (*13*). In contrast, our study not only identifies citrate as a key upstream regulator of

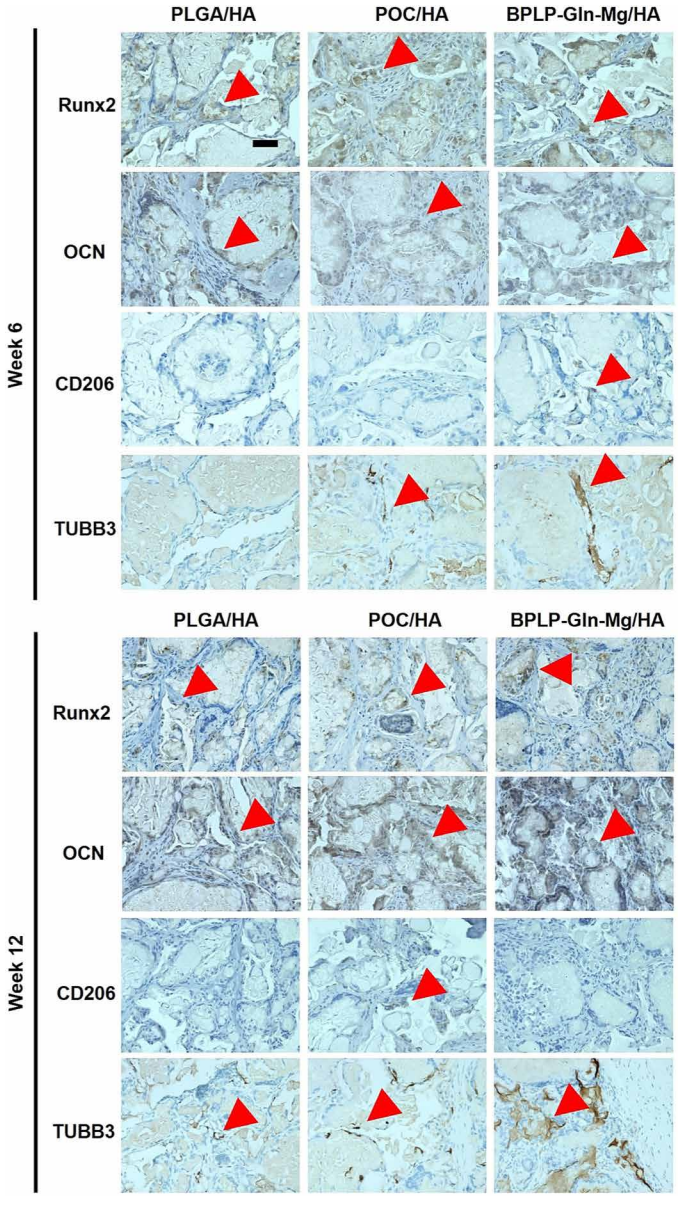

Fig. 9. Immunohistochemistry staining of OCN, Runx2, CD206, and TUBB3 at the defect site at week 6 and week 12. Red arrow indicates representative area with positive staining. Scale bar, 50 μm.

mTORC1-AMPK dual activation but also demonstrates that, when combined with glutamine and magnesium, this effect is sustained over time and supports the prolonged metabolic demands of osteogenesis. This functionalization translates molecular signaling into tissue-level outcomes, enhanced bone formation, broadening therapeutic implications of concurrent mTORC1 and AMPK activation. CaMKK2-mediated AMPK activation emerges as a calcium-dependent process that does not rely on fluctuations in AMP or ADP levels (*25*). Citrate, glutamine, and magnesium supplementation were shown to elevate intracellular calcium levels, triggering CaMKK2 signaling. Concurrently, the AKT-mTORC1 axis is dominant in overriding AMPK's inhibitory influence during osteogenesis. These observations are consistent with previous studies demonstrating the critical role of the AKT-mTORC1 pathway in promoting osteoblast differentiation. The inhibition of CaMKK2 or AKT in our experiments disrupted the osteogenic effects of citrate, glutamine, and magnesium, underscoring the importance of these upstream regulators. Notably, our findings indicate the critical role of intracellular calcium in promoting bone regeneration. However, the combination of citrate, glutamine, and magnesium not only activates the CaMKK2-AMPK pathway through calcium-mediated stimulation but also enhances oxidative phosphorylation, as evidenced by increased oxygen consumption, mitochondrial membrane potential, and TCA cycle activity. Concurrently, the combination further promotes AKT-mTORC1 signaling, indicating coordinated activation of both energy-sensing and growth-promoting pathways. Calcium, primarily delivered through HA, is incorporated at ~20 wt % in the CitraBoneQMg composite. Despite the presence of HA, CitraBoneQMg significantly outperformed PLGA/HA and POC/HA in promoting bone regeneration, demonstrating that calcium alone is insufficient. Instead, the synergistic regulation of metabolic and signaling pathways by citrate, glutamine, and magnesium is essential for optimal bone healing. However, the underlying mechanism behind the increase in intracellular calcium levels induced by citrate, glutamine, and magnesium remains unexplored and should be further investigated in future studies.

The transition from glycolysis to OXPHOS during osteogenic differentiation is a hallmark of the metabolic shift that occurs in differentiating human MSCs (*52*). This metabolic reprogramming ensures adequate ATP production to support the energy-intensive processes involved in osteoblast maturation, extracellular matrix synthesis, and mineralization. Citrate, glutamine, and magnesium supplementation enhance mitochondrial function by increasing ATP levels, OCRs, and mitochondrial membrane potential, reinforcing the energy supply needed for osteogenesis. Metabolomic analyses further revealed an upregulation of TCA cycle intermediates, confirming that these supplements replenish the TCA cycle and enhance its central role as a metabolic hub (*19*).

Beyond their effects on the TCA cycle, we found citrate, glutamine, and magnesium also modulate other metabolic pathways critical to osteogenesis, such as nucleotide and amino acid metabolism. The TCA cycle intermediates, such as α-ketoglutarate and oxaloacetate, serve as precursors for nucleotide synthesis, which supports the increased demand for DNA synthesis during early osteoblast differentiation when cells are rapidly proliferating. In addition, amino acid metabolism contributes to protein synthesis, redox balance, lipid biosynthesis, and epigenetic modifications (*53*). These findings align with previous studies that have demonstrated the essential roles of amino acids in promoting skeletal cell function and bone regeneration (*54*–*58*). Collectively, these results indicate that citrate, glutamine, and magnesium act as metabolic regulators that facilitate multiple biosynthetic processes essential for osteogenesis.

To translate these findings into practical applications, we developed CitraBoneQMg, a bioactive composite comprising citrate, glutamine magnesium, and HA. This biomaterial was designed to provide structural support while creating an osteogenic microenvironment through the sustained release of bioactive components. In vitro studies demonstrated that CitraBoneQMg significantly enhances osteogenic differentiation, as evidenced by the elevated expression of osteogenic genes, increased ALP activity, and enhanced calcium nodule formation. These effects are attributed to the synergistic action of citrate, glutamine, and magnesium in promoting mTORC1 and AMPK activities while fulfilling the energy demands of osteogenesis.

The in vivo efficacy of CitraBoneQMg was validated in a rat calvarial defect model, where it outperformed the well-known POC/HA and PLGA/HA composites in promoting bone formation and maturation. Histological analyses revealed that CitraBoneQMg implants facilitated earlier and more robust bone regeneration, with significant increases in new and mature bone formation observed at both 6 and 12 weeks post-implantation. In addition, CitraBoneQMg accelerated the transition to the reparative stage by promoting M2 macrophage polarization, as indicated by the earlier expression of CD206 compared to POC/HA. This finding aligns with the anti-inflammatory properties of glutamine and magnesium, while citrate's role in immunomodulation is gaining increasing attention (*3*, *59*–*63*). Metabolomic analyses suggest that citrate supplementation elevates acetyl–coenzyme A (CoA) levels, which are linked to M2 macrophage function through histone acetylation and gene expression regulation (*60*). Notably, despite the cytotoxicity exhibited at 1× dilution of leachant and fully degraded products in cell culture (fig. S10), BPLP-Gln-Mg/HA not only demonstrated superior bone regeneration compared to POC/HA but also showed no signs of biosafety issues. Unlike the static exposure in cell culture assays, the gradual 20-week degradation of BPLP-Gln-Mg and dynamic fluid circulation in vivo minimize local concentration spikes and mitigate potential toxicity.

The nervous system in bone regeneration is often overlooked but is critical for successful tissue repair (*64*–*66*). Our study demonstrated that CitraBoneQMg enhances TUBB3 expression, indicating improved nerve regeneration during bone healing. Citrate's role in Schwann cell function and myelination has been previously documented, suggesting its potential to support peripheral nerve repair (*67*). Schwann cells undergo metabolic reprogramming during differentiation, shifting from glycolysis to oxidative metabolism. Citrate supplementation rescues defects in Schwann cell function by restoring citrate synthase activity, emphasizing its role in promoting reinnervation during bone repair. Future studies should investigate whether exogenous citrate can directly enhance Schwann cell function and reinnervation in bone regeneration models.

Metabolism-regulating biomaterials represent a novel and clinically significant advancement in orthopedic engineering, shifting the paradigm from traditional bioactive materials—which passively support tissue regeneration—to dynamic platforms that actively modulate intracellular metabolic activity. Unlike conventional approaches that rely on the release of growth factors (*68*, *69*), cell-derived exosomes (*69*), or even the direct incorporation of live cells (*69*), these next-generation biomaterials engage specific metabolic pathways, such as oxidative phosphorylation and the TCA cycle, to boost ATP production, enhance biosynthesis, and regulate osteogenic signaling. This metabolic reprogramming enables more precise control over cell fate and regenerative outcomes and is particularly advantageous for treating large bone defects or patients with compromised healing capacity. In addition, these materials offer a cost-effective, off-the-shelf solution with strong translational potential from bench to bedside. Recent studies have demonstrated the efficacy of biomaterials that release TCA cycle metabolites—such as citrate (*24*), α-ketoglutarate (*2*), succinate (*1*), and malate (*70*)—in enhancing ATP production and promoting tissue regeneration. Extending beyond TCA cycle metabolites, our study provides a comprehensive understanding of the synergistic effects of a metabolite (citrate), an amino acid (glutamine), and a metal ion (magnesium) on cellular metabolism and signaling pathways critical for osteogenesis. We translated these mechanistic insights into the rational design of CitraBoneQMg, a bioactive material capable of delivering these components in a controlled manner and modulating the local cellular microenvironment to promote robust bone regeneration.

While this study provides insights into the roles of citrate, glutamine, and magnesium in osteogenesis, further research is needed to address several unanswered questions. The mechanisms through which these supplements elevate intracellular calcium levels remain unclear and warrant further investigation. In addition, citrate's involvement in epigenetic regulation through histone acetylation offers a promising avenue for understanding how it influences gene expression during osteogenesis (*71*). As citrate serves as a precursor to acetyl-CoA, its role in restoring histone acetylation and reversing osteogenic defects in aged MSCs could provide valuable insights for developing therapeutic strategies for age-related bone disorders (*72*). Last, understanding whether the degradation products of CitraBoneQMg retain their metabonegenic properties could guide the optimization of citrate-based biomaterials for clinical applications.

In conclusion, this study establishes citrate, glutamine, and magnesium as multifaceted regulators of osteogenesis, integrating energy metabolism with signaling pathways to meet the metabolic demands of bone regeneration. The CitraBoneQMg biomaterial offers structural and metabolic support, significantly enhancing bone repair in vivo, promoting multi-tissue regeneration by coordinating the activity of bone, immune, and neural system—an integrated process we term "metabotissugenesis," which we have a thorough discussion in our recent review article (*5*). These findings lay the groundwork for future advancements in citrate-based biomaterials, emphasizing their translational potential for orthopedic applications. By addressing the metabolic and signaling needs of osteogenesis, CitraBoneQMg represents a critical step forward in the design and development of next-generation biomaterials for bone tissue engineering.

MATERIALS AND METHODS

Cell culture and osteogenic differentiation

The following procedures were previously described (*24*). Briefly, hBM-MSCs were obtained from American Type Culture Collection and maintained in growth medium (GM) [low-glucose Dulbecco's modified essential medium (DMEM) (Sigma-Aldrich) containing 10% fetal bovine serum (FBS)] at 37°C in 5% CO_2 (v/v) in a humidified incubator. The GM medium was replaced every 2 days. To initiate the osteogenic differentiation, cells at ~80% confluence were treated with an established osteogenic (OG) medium (low-glucose DMEM with 10^{-7} M dexamethasone, 0.05 mM ascorbate-2-phosphate, and 0.01 M β-glycerophosphate). The OG medium was replaced every 3 days. hBM-MSCs were incubated with OG medium with various concentrations of citrate, glutamine, and magnesium at indicated times. In some experiments, hBM-MSCs were pretreated with Torin1 (100 nM), STO-609 (32 μM), or MK-2206 (1 μM) for 1 hours before OG medium ± citrate, glutamine, and magnesium.

Proliferation assay

hBM-MSCs were seeded at 5000 cells/cm^2, various concentrations of glutamine or magnesium were added the next day, and Cell Counting Kit-8 (CCK-8) assay (Dojindo) was used according to manufacturing protocol to determine cell viability at determined times.

ALP assay and DNA quantification

The following procedures were previously described (*24*). Briefly, to analyze ALP expression, cells were lysed with radioimmunoprecipitation assay (RIPA) buffer on day 7 of osteogenic differentiation, followed by centrifugation to remove debris. ALP activity was then measured using *p*-nitrophenyl phosphate (PNPP), which ALP hydrolyzes to produce a yellow-colored product. Briefly, a 1 M PNPP stock solution was diluted 1:100 with ALP assay buffer, and 50 μl of this solution was added to 50 μl of the lysate sample. After incubating at 37°C for 10 to 30 min, absorbance was measured at 405 nm using a plate reader (Tecan). The same lysate samples were also used to quantify DNA content using the PicoGreen dsDNA Quantification Kit (Invitrogen), following the manufacturer's instructions.

Alizarin Red staining and calcium quantification

The following procedures were previously described (*24*). Briefly, for Alizarin Red staining, cells were fixed with 4% paraformaldehyde, and 40 mM Alizarin red solutions were used to stain calcium nodules for 30 min with gentle shaking. After thoroughly washing, the stained cells were observed on a microscope (Nikon). The same cell samples were used to quantify calcium using Alizarin Red S Staining Quantification Assay (ScienCell) following the manufacturer's protocol. Briefly, 10% acetic acid was added to cell samples and incubated at room temperature for 30 min with shaking. Cell samples were scraped and collected into 1.5-ml microcentrifuge tubes. Cell samples were heated at 85°C for 10 min and then incubated on ice for 5 min. Then, cell samples were centrifuged at 20,000*g* for 15 min. Supernatants were collected, and 10% ammonium hydroxide was added to neutralize the acid. Absorbance was measured at 405 nm using a plate reader (Tecan).

Real-time PCR

The following procedures were previously described (*24*). Briefly, total RNA from whole cells was isolated with Zymo Direct-zol RNA Microprep kit and was transcribed into cDNA using Invitrogen SuperScriptIII First-Strand Synthesis System. For quantitative analysis, real-time polymerase chain reaction (PCR) was performed using cDNA as the template, together with TaqMan Gene Expression Master Mix and the TaqMan Gene Expression Assays with both primers and probe included (Applied Biosystems), and using the StepOnePlus Real-Time PCR system (Applied Biosystems) according to the manufacturer's instructions. Human peptidylprolyl isomerase A (PPIA; cyclophilin A) was used for normalization.

Immunofluorescent staining

The following procedures were previously described (*24*). Briefly, for ALP and OPN expression analysis, hBM-MSCs differentiated for 14 days were fixed with 4% paraformaldehyde. After washing with PBS, cells were blocked using 0.1% Triton X-100 in phosphate-buffered saline (PBST) with 1% bovine serum albumin (BSA) at room temperature for 1 hour. Then, mouse anti-ALP primary antibody (Santa Cruz Biotechnology) and mouse anti-OPN primary antibody (Santa Cruz Biotechnology) at 1:500 diluted with blocking buffer was added to samples and incubated overnight at 4°C. Mouse IgGk light chain binding protein (m-IgGk BP) conjugated to CruzFluor 555 (m-IgGκ BP-CFL 555; Santa Cruz Biotechnology) and m-IgG BP-CFL 488 (Santa Cruz Biotechnology)–labeled secondary antibody 1:100 diluted with blocking buffer for 1 hour. Subsequently, The 4′,6-diamidino-2-phenylindole (DAPI) solution was applied to stain the cell nucleus, and the stained cells were observed and recorded on a fluorescence microscope (Nikon)

Intracellular ATP level analysis

To measure the intracellular ATP level for undifferentiated hBM-MSCs, cells were seeded at 10,000 cells/cm^2 and treated with citrate, glutamine, and/or magnesium for 24 hours the next day. For osteogenic differentiating hBM-MSCs, cells were treated with citrate, glutamine, and/or magnesium for 7 days. Cells were collected and measured using ATPlite 1step (Revvity) according to the manufacturer's protocol.

XF bioenergetic analysis

OCRs were measured using the SeahorseXF24 instrument (Agilent) according to the manufacturer's protocols. hBM-MSCs were seeded in a XF24 microplate at a density of 20,000 cells per well in 200 μl of GM. Citrate, glutamine and magnesium were applied the next day in OG medium. On day 7, cells were treated with XF assay medium (pH 7.4) supplemented with 5.5 mM glucose, 1 mM sodium pyruvate, and 0.5 mM glutamine for 60 min in a 37°C non-CO_2 incubator; sensor cartridges were hydrated 1 day before the start of assays. Injections of 1.5 μM oligomycin, 4 μM carbonyl cyanide *p*-trifluor omethoxyphenylhydrazone, and 0.5 μM rotenone/antimycin A were used to analyze mitochondria response. All the reagents were from Agilent Technologies (Seahorse Biosciences).

Mitochondrial membrane potential fluorescence staining

Mitochondrial membrane potential was analyzed using Mitochondrial Membrane Potential Assay Kit (II) (Cell Signaling Technology) based on manufacturing protocol. Briefly, hBM-MSCs were plated in glass bottomed culture dishes at 8000 cells/cm^2 with GM medium containing 0.5 mM glutamine. At 80 to 90% confluence, cells were treated with citrate, glutamine, and magnesium at various combinations in OG medium. On day 3, 200 nM tetramethylrhodamine, ethyl ester (TMRE) labeling solution were added and incubated (37°C and 5% CO_2) for 20 min. Cells were washed three times with 1× PBS and hydrated in 1× PBS for imaging. Images were captured at ×63 magnification using Zeiss LSM 880 Confocal with fluorescence lifetime imaging microscopy.

Western blotting

The following procedures were previously described (*24*). Briefly, dialyzed FBS (10%) (Cytiva) was used in OG medium. On day 3 of OG differentiation, cells were treated with citrate, glutamine, and magnesium. For some experiments, cells were treated with inhibitors before citrate, glutamine, and magnesium treatments. After 4 hours of treatment, cells were washed with ice-cold PBS and then collected with ice-cold RIPA with protease inhibitor and phosphatase inhibitor at 1:100 and 1:50 dilution, respectively. Lysates were incubated for 10 min at 4°C with gentle agitation and then centrifuged at 16,000*g* at 4°C for 15 min to remove insoluble debris. After protein quantification by bicinchoninic acid (BCA) assay (Thermo Fisher Scientific), gel electrophoresis was carried out on AnykDTM Mini-Protean TGX stain-free protein gels at 50 V for 10 min, followed by 150 V for 30 to 60 min and was transferred to nitrocellulose membranes with the Trans-Blot TurboTM system. Then, membranes were blocked with TBST–5 wt % nonfat milk at room temperature for 1 hour and then incubated with primary antibodies overnight at 4°C in TBST−5 wt % BSA. After washing with TBST

five times for 5 min, the membranes were incubated in the horseradish peroxidase (HRP)–conjugated secondary antibody solution diluted in TBST–5 wt % nonfat milk for 1 hour at room temperature, followed by rinsing and incubating with ClarityTM western enhanced chemiluminesence substrate mixture for 5 min, and then imaged by the ChemiDoc MP imaging system (Bio-Rad).

Metabolomics

On day 3 of osteogenic differentiation, cells were snap-frozen with liquid nitrogen. A 90% HPLC-grade methanol/water was then added immediately after liquid nitrogen evaporated. Cells were scraped with a cell lifter and collected into micro-centrifuge tubes, then vortexed to resuspend the cells, and centrifuged for 15 min at 15,000 rpm at 4°C. Supernatants were collected and speed vacuum to dry the samples. Metabolite pellets were resuspended in 3% HPLC-grade methanol:water containing 1 μM chlorpropamide. Samples were vortexed and centrifuged for 15 min at 15,000 rpm at 4°C. Supernatants were collected for analysis using Thermo Exactive Plus.

Metabolomics data analysis

Data were converted using MSConvert and extracted using El-Maven, and the signal-to-noise ratio was set as 3. Using the R language platform (R Foundation for Statistical Computing; www.r-project.org), identical metabolites' intensity (peak area) values were aggregated, regardless of their ionization format. This method allows for a robust assessment of metabolite levels across multiple samples. Through manual curation, we ensured that all metabolites were consistently assigned a unique Kyoto Encyclopedia of Genes and Genomes (KEGG) compound ID to facilitate subsequent downstream analyses. Metabolites with maximum values in the samples lower than those in the blank samples were filtered out.

The normalization process involved calculating a scale factor from the intensity of chlorpropamide, used as an internal control. This scale factor was determined by dividing the control intensity values by their means. Subsequently, the intensity data were normalized by dividing each sample's intensity by the corresponding scale factor. Last, a log 2 transformation was applied to the normalized data, with one added to avoid taking the logarithm of zero.

Log-normalized metabolome data were then used to conduct principal components analysis (PCA) analysis and group difference tests. Based on the results of the homogeneity of variance test (Bartlett test), analysis of variance (ANOVA), or Kruskal's test was used to evaluate group differences accordingly. Post hoc comparisons were performed using Tukey's post hoc or Dunn's test. In addition, the Benjamini-Hochberg method was applied to control the false discovery rate (FDR).

Differential metabolites (DM) were filtered based on adjusted p-values obtained from the pairwise comparisons and the fold change of metabolite intensity, using $P_{adj} < 0.05$ and |fold change| >1.2.

scRNA-seq data analysis

scRNA-seq data of non-hematopoietic cells of hBM were downloaded from National Center for Biotechnology Information (NCBI) Gene Expression Omnibus (GEO) (GSE253355). Based on the results presented in the previous research, Osteo-MSCs, $APOD^+$ MSCs, and osteoblasts were extracted, corresponding to the "osteogenic populations" (*73*).

All samples were merged and processed through log-normalization, followed by the identification of the top 2000 features. The data were subsequently scaled, and PCA was performed. To address batch effects among individual samples, single-cell data were integrated using the *simspec::cluster_sim_spectrum* function with parameters set to $k = 5$ and *cluster_resolution* = *0.5*, while the remaining parameters were maintained at their default values (*74*). Furthermore, the cell populations with high expressions of COL1A1 and ALPL within osteoblasts were identified separately as osteocytes. Last, the integrated dataset was visualized using UMAP. The osteogenesis trajectory and pseudotime were inferred by Slingshot using embeddings from UMAP (*75*).

Intracellular calcium fluorescent staining

hBM-MSCs were plated in glass bottomed culture dishes at 8000 cells/cm^2 with GM medium containing 0.5 mM glutamine. At 90% confluence, cells were treated with citrate, glutamine, and magnesium in various combinations for 3 days in the OG medium. Cells were stained with Oregon Green 488 BAPTA-1, AM (Thermo Fisher Scientific) based on manufacturing protocol. Briefly, cells were incubated with the AM ester for 1 hour at room temperature. Cells were then washed thoroughly to remove excess probe. Images were captured at ×10 magnification using a fluorescence microscope (Nikon).

Intracellular citrate, glutamine and magnesium concentrations

hBM-MSCs were treated with citrate, glutamine, or magnesium supplementations during osteogenic differentiation for 3 days. On day 3, cells were lysed with RIPA. Intracellular citrate concentrations were measured using the EnzyChrom Citrate Assay Kit (BioAssay Systems) according to the manufacturer's protocol. Intracellular glutamine was analyzed using metabolomics (see the "Metabolomics" section). Intracellular magnesium concentrations were measured using the QuantiChrom Magnesium Assay Kit (BioAssay Systems) according to the manufacturer's protocol.

Synthesis of prepolymers

The following procedures were previously described (*24*). Briefly, for BPLP-Gln synthesis, citric acid, 1,8-octanediol, and L-glutamine at molar ratios of 1:1.1:0.3 and 1:1.1:0.5 were mixed in a round-bottomed flask. After melting at 160°C for 20 min, the temperature was lowered to 140°C, and the mixture was stirred continuously for another 50 min with the stirring speed lowering gradually from 800 to 80 rpm to produce the BPLP-Gln prepolymer. The prepolymer was then dissolved in 1,4-dioxane and purified by precipitation in water, followed by freeze drying. For BPLP-Gln-Mg prepolymers synthesis, the same steps were followed as above until the temperature was lowered to 140°C, and magnesium nitrate hexahydrate was added at molar ratios of 0.1, 0.2 and 0.3 and continued with the same steps as mentioned above.

Preparation of polymer films and composites

The following procedures were previously described (*24*). Briefly, to prepare polymer films, POC, BPLP-Gln, and BPLP-Gln-Mg prepolymers were dissolved in 1,4-dioxane to form a 30 wt % solution and then cast into a Teflon dish for solvent evaporation and thermal cross-linking at 80°C for 3 days, followed by 120°C for another 3 days. For composites, a 30 wt % prepolymer solution was mixed with 50 wt % HA and stirred in Teflon dishes to achieve a homogeneous mixture. After solvent evaporation, the composite was rolled and pressed into thin sheets using a pasta roller machine, cut into round

disks, and cross-linked under the same thermal conditions (80°C for 3 days and then 120°C for 3 days).

FTIR and NMR analysis

For H nuclear magnetic resonance (NMR) analysis, 5 mg of polymer was dissolved in 1 ml of deuterated dimethyl sulfoxide (DMSO-d6; Sigma-Aldrich), and the H-NMR was recorded on a Bruker Advance 600 NMR spectrometer (Bruker). Polymer films were cut into small square shapes, and FTIR was recorded on a Bruker Vertex 80 spectrometer (Bruker).

Determination of released concentrations of citrate, glutamine, and magnesium

The following procedures were previously described (*24*). Briefly, HPLC (Shimadzu) was performed to confirm the presence of citrate and glutamine in polymer films. To prepare, 10 ml of PBS was added into 0.5 g of polymer films. PBS was collected and changed for every determined day. The collected samples were filtered through a 0.2-μm filter before running HPLC. HPLC analysis was performed on a Shimadzu HPLC system equipped with an ultraviolet-visible photo diode array (PDA) detector and a C18 column at room temperature. The detection of citrate and glutamine was set at 210 and 207 nm, respectively, and the calibration curves of citrate and glutamine were obtained. For Mg^{2+} release studies, samples were analyzed by inductively coupled plasma-atomic/optical emission spectrometry, on a Thermo iCAP 7400 Duo instrument with Qtegra software. Calibration standards were purchased from High-Purity Standards (North Charleston). The iCAP Duo allows analyzing elements in both axial and radial views to encompass a wide range of concentrations. Approximately 5 ml of each sample was analyzed. Mg^{2+} was measured at 285.213 nm in both axial and radial view.

Photoluminescent and photoacoustic properties of BPLP-Gln-Mg

The following procedures were previously described (*76*). Briefly, the photoluminescent properties of the polymers were analyzed using a Horiba FluoroMax-4 spectrofluorometer (Horiba Scientific). Unless otherwise specified, both the excitation and emission slit widths were set to 1.5 nm for all samples. Photostability was assessed by monitoring the emission intensity decay at the maximum excitation and emission wavelengths under continuous illumination for 3 hours in the spectrofluorometer. For photoacoustic imaging, samples were placed in a 1.5 wt % agarose phantom and imaged using the Acoustic X (7 MHz) probe to collect photoacoustic images at multiple wavelengths ranging from 700 to 900 nm. The samples were placed in a line perpendicular to the 128 array elements of the transducer to expose each film sequentially to the optical fibers.

Degradation studies

For degradation studies under neutral conditions, polymer films were cut into round disks (~50 mg, 8 mm diameter, ~1 mm thickness) and placed in tubes containing 10 mL of PBS (pH 7.2–7.4). Samples were incubated at 37°C for predetermined times, with daily PBS changes until the pH stabilized at 7.4, followed by weekly changes. At each time point, samples were removed, thoroughly washed with deionized water, and lyophilized. Degradation was assessed by measuring the remaining mass using the equation

$$W1 / W0 \times 100\%$$

where $W0$ is the initial film weight and $W1$ is the remaining weight.

Cytocompatibility evaluation of leachant and degraded products

To prepare liquid extracts of polymer films, POC, BPLP-Gln, and BPLP-Gln-Mg films were cut into round disks sized for a 24-well plate. Complete culture medium was then added, and the films were incubated at 37°C with agitation for 24 hours following the ISO 10993-5:2009(E) standard. The resulting liquid extracts were collected, filtered, and applied to L929 cells at 80 to 90% confluence in 96-well plates. After a 24-hour incubation, cell viability was assessed using the CCK-8 assay (Dojindo).

To prepare degradation products, 0.5 g of polymer films were fully degraded in 3 ml of 2 N NaOH solution. The pH was adjusted to 7.2 to 7.4 using 2 N HCl, and the final volume was brought to 5 ml with deionized water. After centrifugation, the supernatant was filtered into a separate tube. Serial dilutions of the degradation products were prepared using culture medium, and 20 μl of each dilution was added to cells cultured in 96-well plates with 200 μl of medium. Following a 24-hour incubation, cell viability was evaluated using the CCK-8 assay (Dojindo) according to the manufacturer's instructions.

In vitro biological evaluation of composites and SEM observation

To assess the bioactivity of the composites, hBM-MSCs were seeded at a density of 10,000 cells/cm^2 in GM medium. After 5 days of culture, the cells were treated with OG medium for 7 days and then collected for ALP activity and gene expression analysis. For calcium nodule formation analysis, cells cultured for 21 days were collected and examined using field-emission SEM (Zeiss Sigma) equipped with energy-dispersive EDS after sputter coating with iridium (Emitec Sputter-Coater). Elemental data were acquired at 10 kV from areas of interest and analyzed using AZtec software (Oxford Instruments).

Immune evaluation of composites

Immune evaluation of polymer composites with Raw 264.7 cells was performed. Briefly, Raw 264.7 cells at 10,000 cells/cm^2 were seeded on composites disks (POC, BPLP-0.3Gln-Mg, and BPLP-0.5Gln-Mg) with the diameter of 10 mm in 48-well plates. Cells were incubated with high glucose DMEM supplemented with 10% FBS and 1% antibiotics. After 72 hours, the cell suspension of each sample was collected and centrifuged at 1500 rpm for 5 min. The supernatant was collected to determine the IL-10 concentrations using an ELISA kit (R&D Systems). The remaining composites with cells were collected and imaged with SEM.

Mechanical testing

The following procedures were previously described (*24*). Briefly, to evaluate the compressive strength of polymer/HA composites, cylindrical samples were prepared by mixing prepolymers with 50 wt % HA. Once the polymer-HA mixtures reached a clay-like consistency, they were molded into polytetrafluoroethylene tubing and post-polymerized at 80°C for 3 days, followed by 120°C for another 3 days. Compression testing was then conducted on the cylindrical specimens using an Instron 5966 machine equipped with a 10-kN load cell (Instron) at a strain rate of 1.3 mm/min until failure. The initial

modulus was determined by calculating the slope of the stress-strain curve at 10% compression.

Rat critical-sized calvarial defect

The following procedures were previously described (*24*). Briefly, all animal experiments were conducted in accordance with protocols approved by The Pennsylvania State University's Institutional Animal Care and Use Committee (protocol number 42878). Male Sprague-Dawley rats (8 weeks old) were used for the study. Surgeries were performed under continuous isoflurane anesthesia. Buprenorphine (1 mg/kg) was administered subcutaneously for analgesia. The surgical site was shaved and disinfected with a 70% ethanol solution, followed by a subcutaneous injection of bupivacaine (4 mg/kg) as a local anesthetic.

A sagittal incision (1.5 to 2 cm) was made from the nasal bone to the middle sagittal crest, and the periosteum was bluntly dissected. A 5-mm-diameter calvarial defect was created using a trephine drill, continuously irrigated with sterile saline to prevent heat damage. The calvarial disk was carefully removed to avoid dural tears, and implants were inserted into the defects via press-fit placement. The periosteum and skin were sutured with 4-0 vicryl, and animals were monitored according to standard post-operative care protocols. After 6- and 12-weeks post-surgery, animals were anesthetized and euthanized, and the skulls were collected for micro-CT imaging, histochemistry, and immunostaining analysis.

Micro-CT analysis

The following procedures were previously described (*24*). Briefly, the skulls were fixed with 4% paraformaldehyde overnight and rinsed with PBS. Then, the skulls were evaluated via isolated bone mode using the GE Pheonix v|tome|x L at 150 kV with an integration time of 333 ms for each of the 360 rotational steps. Slices (2150) with resolutions of 20 μm were collected, and the reconstructed dataset was segmented by an automated thresholding algorithm. General Electric (GE) proprietary reconstruction software was used to reconstruct the 3D image. The volume of interest was defined as a hollow cylinder of a height that could cover the entire thickness of the defect, and the BV/TV was calculated using AVIZO. BMD among groups was calculated using ImageJ.

Histological analysis

The fixed skulls were decalcified with 0.5 M EDTA at pH 7.4 at 4°C for 4 to 7 weeks and embedded in paraffin. Tissues were sectioned with a 5-μm thickness, dewaxed, rehydrated, and stained with H&E and Masson's trichrome for light microscopic analysis. Images were captured at ×20 magnification using a Keyence BZ-9000 E Microscope.

Immunohistochemical analysis

To detect OCN, Runx2, CD206, and TUBB3 expressions, paraffin-embedded sections were dewaxed (Leica Autostainer ST5010 XL). Antigen was retrieved using a pH 6 buffer. Then, the sections were blocked with 5% normal goat serum for 1 hour and incubated with the primary anti-OCN antibody (1:50; Proteintech), anti-Runx2 antibody (1:50 dilution; Thermo Fisher Scientific; 1:50 dilution), anti-CD206 antibody (1:50; Cell Signaling Technology), and anti-TUBB3 antibody (1:50; Invitrogen) at 4°C overnight. The sections were washed with TBS three times, and endogenous peroxidase activity was blocked by 3% hydrogen peroxide. Then, the slides were incubated with secondary HRP-Goat anti-mouse IgG_1 (1:200 dilution; Thermo Fisher Scientific) or HRP-Goat anti-rabbit IgG (1:200 dilution; Invitrogen) for 1 hour at 37°C. Colorization was subsequently developed in DAB solution (Thermo Fisher Scientific) and counterstained. Images were captured at ×20 magnification using a Keyence BZ-9000 E Microscope.

Fluorescent imaging of tissue sections

Palin tissue slides were imaged using Keyence BZ-9000 E Microscope under green fluorescent protein (GFP) fluorescence. Images were captured at ×4 magnification.

Statistical analysis

All quantitative data are presented as means ± SD with a minimum of three independent samples. Statistical analyses were performed using Prism GraphPad software, and ordinary one-way ANOVA was performed on three or more groups with the Tukey's post hoc test applied within groups. A one-tailed unpaired *t* test was applied when only two groups were compared. *P* values < 0.05 were regarded as statistically significant. $^{*}P < 0.05$, $^{**}P < 0.005$, $^{***}P < 0.0005$, and $^{****}P < 0.0001$.

Supplementary Materials

The PDF file includes:
Figs. S1 to S12
Legend for table S1

Other Supplementary Material for this manuscript includes the following:
Table S1

REFERENCES AND NOTES

1. H. Liu, Y. Du, J.-P. St-Pierre, M. S. Bergholt, H. Autefage, J. Wang, M. Cai, G. Yang, M. M. Stevens, S. Zhang, Bioenergetic-active materials enhance tissue regeneration by modulating cellular metabolic state. *Sci. Adv.* **6**, eaay7608 (2020).
2. Z. Wang, J. Hu, J. S. Marschall, L. Yang, E. Zeng, S. Zhang, H. Sun, Antiaging metabolite-based polymeric microparticles for intracellular drug delivery and bone regeneration. *Small Sci.* **4**, 2400201 (2024).
3. W. Qiao, K. H. M. Wong, J. Shen, W. Wang, J. Wu, J. Li, Z. Lin, Z. Chen, J. P. Matinlinna, Y. Zheng, S. Wu, X. Liu, K. P. Lai, Z. Chen, Y. W. Lam, K. M. C. Cheung, K. W. K. Yeung, TRPM7 kinase-mediated immunomodulation in macrophage plays a central role in magnesium ion-induced bone regeneration. *Nat. Commun.* **12**, 2885 (2021).
4. C. Ma, M. L. Kuzma, X. Bai, J. Yang, Biomaterial-based metabolic regulation in regenerative engineering. *Adv. Sci.* **6**, 1900819 (2019).
5. H. Xu, S. Yan, E. Gerhard, D. Xie, X. Liu, B. Zhang, D. Shi, G. A. Ameer, J. Yang, Citric acid: A nexus between cellular mechanisms and biomaterial innovations. *Adv. Mater.* **36**, e2402871 (2024).
6. J. Zhu, C. B. Thompson, Metabolic regulation of cell growth and proliferation. *Nat. Rev. Mol. Cell Biol.* **20**, 436–450 (2019).
7. R. A. Saxton, D. M. Sabatini, mTOR signaling in growth, metabolism, and disease. *Cell* **168**, 960–976 (2017).
8. M. M. Mihaylova, R. J. Shaw, The AMPK signalling pathway coordinates cell growth, autophagy and metabolism. *Nat. Cell Biol.* **13**, 1016–1023 (2011).
9. A. González, M. N. Hall, S.-C. Lin, D. G. Hardie, AMPK and TOR: The yin and yang of cellular nutrient sensing and growth control. *Cell Metab.* **31**, 472–492 (2020).
10. J. Chen, F. Long, mTOR signaling in skeletal development and disease. *Bone Res.* **6**, 1 (2018).
11. L. Xian, X. Wu, L. Pang, M. Lou, C. J. Rosen, T. Qiu, J. Crane, F. Frassica, L. Zhang, J. P. Rodriguez, X. Jia, S. Yakar, S. Xuan, A. Efstratiadis, M. Wan, X. Cao, Matrix IGF-1 maintains bone mass by activation of mTOR in mesenchymal stem cells. *Nat. Med.* **18**, 1095–1101 (2012).
12. S. Chava, S. Chennakesavulu, B. M. Gayatri, A. B. M. Reddy, A novel phosphorylation by AMP-activated kinase regulates RUNX2 from ubiquitination in osteogenesis over adipogenesis. *Cell Death Dis.* **9**, 754 (2018).
13. P. Dalle Pezze, S. Ruf, A. G. Sonntag, M. Langelaar-Makkinje, P. Hall, A. M. Heberle, P. Razquin Navas, K. Van Eunen, R. C. Tölle, J. J. Schwarz, H. Wiese, B. Warscheid, J. Deitersen, B. Stork, E. Fäßler, S. Schäuble, U. Hahn, P. Horvatovich, D. P. Shanley, K. Thedieck, A systems study reveals concurrent activation of AMPK and mTOR by amino acids. *Nat. Commun.* **7**, 13254 (2016).

14. A. Y. Clark, K. E. Martin, J. R. García, C. T. Johnson, H. S. Theriault, W. M. Han, D. W. Zhou, E. A. Botchwey, A. J. García, Integrin-specific hydrogels modulate transplanted human bone marrow-derived mesenchymal stem cell survival, engraftment, and reparative activities. *Nat. Commun.* **11**, 114 (2020).
15. W. Lin, Q. Li, L. Liu, Q. Wang, D. Zhang, F. Wang, R. Xu, Y. Fan, M. Xing, C. Zhou, Q. Yuan, Early infiltrating NKT lymphocytes attenuate bone regeneration through secretion of CXCL2. *Sci. Adv.* **10**, eadl6343 (2024).
16. H. Wang, J. Tian, Y. Jiang, S. Liu, J. Zheng, N. Li, G. Wang, F. Dong, J. Chen, Y. Xie, Y. Huang, X. Cai, X. Wang, W. Xiong, H. Qi, L. Yin, Y. Wang, X. Sheng, A 3D biomimetic optoelectronic scaffold repairs cranial defects. *Sci. Adv.* **9**, eabq7750 (2023).
17. M. Zhang, R. Lin, X. Wang, J. Xue, C. Deng, C. Feng, H. Zhuang, J. Ma, C. Qin, L. Wan, J. Chang, C. Wu, 3D printing of Haversian bone–mimicking scaffolds for multicellular delivery in bone regeneration. *Sci. Adv.* **6**, eaaz6725 (2020).
18. S. Stegen, G. Carmeliet, Metabolic regulation of skeletal cell fate and function. *Nat. Rev. Endocrinol.* **20**, 399–413 (2024).
19. I. Martínez-Reyes, N. S. Chandel, Mitochondrial TCA cycle metabolites control physiology and disease. *Nat. Commun.* **11**, 102 (2020).
20. H. C. Yoo, Y. C. Yu, Y. Sung, J. M. Han, Glutamine reliance in cell metabolism. *Exp. Mol. Med.* **52**, 1496–1516 (2020).
21. J. L. Kröse, J. H. F. De Baaij, Magnesium biology. *Nephrol. Dial. Transplant.* **39**, 1965–1975 (2024).
22. M. Shah, B. Kola, A. Bataveljic, T. R. Arnett, B. Viollet, L. Saxon, M. Korbonits, C. Chenu, AMP-activated protein kinase (AMPK) activation regulates in vitro bone formation and bone mass. *Bone* **47**, 309–319 (2010).
23. C. M. Karner, S.-Y. Lee, F. Long, Bmp induces osteoblast differentiation through both Smad4 and mTORC1 signaling. *Mol. Cell. Biol.* **37**, e00253–e00216 (2017).
24. C. Ma, X. Tian, J. P. Kim, D. Xie, X. Ao, D. Shan, Q. Lin, M. R. Hudock, X. Bai, J. Yang, Citrate-based materials fuel human stem cells by metabonegenic regulation. *Proc. Natl. Acad. Sci.* **115**, E11741–E11750 (2018).
25. G. R. Steinberg, D. G. Hardie, New insights into activation and function of the AMPK. *Nat. Rev. Mol. Cell Biol.* **24**, 255–272 (2023).
26. C. C. Dibble, L. C. Cantley, Regulation of mTORC1 by PI3K signaling. *Trends Cell Biol.* **25**, 545–555 (2015).
27. R. T. Tran, L. Wang, C. Zhang, M. Huang, W. Tang, C. Zhang, Z. Zhang, D. Jin, B. Banik, J. L. Brown, Z. Xie, X. Bai, J. Yang, Synthesis and characterization of biomimetic citrate-based biodegradable composites: Biomimetic citrate-based biodegradable composites. *J. Biomed. Mater. Res. A* **102**, 2521–2532 (2014).
28. D. Wang, Y. Chen, T. Xia, M. Claudino, A. Melendez, X. Ni, C. Dong, Z. Liu, J. Yang, Citric acid-based intrinsic band-shifting photoluminescent materials. *Research* **6**, 0152 (2023).
29. H. Wang, S. Huddleston, J. Yang, G. A. Ameer, Enabling proregenerative medical devices via citrate-based biomaterials: Transitioning from inert to regenerative biomaterials. *Adv. Mater.* **36**, 2470043 (2024).
30. C. Ma, E. Gerhard, D. Lu, J. Yang, Citrate chemistry and biology for biomaterials design. *Biomaterials* **178**, 383–400 (2018).
31. X. Wang, V. Agrawal, C. L. Dunton, Y. Liu, R. K. A. Virk, P. A. Patel, L. Carter, E. M. Pujadas, Y. Li, S. Jain, H. Wang, N. Ni, H.-M. Tsai, N. Rivera-Bolanos, J. Frederick, E. Roth, R. Bleher, C. Duan, P. Ntziachristos, T. C. He, R. R. Reid, B. Jiang, H. Subramanian, V. Backman, G. A. Ameer, Chromatin reprogramming and bone regeneration in vitro and in vivo via the microtopography-induced constriction of cell nuclei. *Nat. Biomed. Eng.* **7**, 1514–1529 (2023).
32. D. Shan, D. Wang, Y. Ma, Z. Liang, D. J. Ravnic, N. Zhang, J. Yang, Biodegradable citrate-based polymers enable 5D monitoring of implant evolution. *Adv. Funct. Mater.* **35**, 2414400 (2025).
33. X. Tan, E. Gerhard, Y. Wang, R. T. Tran, H. Xu, S. Yan, E. B. Rizk, A. D. Armstrong, Y. Zhou, J. Du, X. Bai, J. Yang, Development of biodegradable osteopromotive citrate-based bone putty. *Small* **18**, e2203003 (2022).
34. J. Guo, X. Tian, D. Xie, K. Rahn, E. Gerhard, M. L. Kuzma, D. Zhou, C. Dong, X. Bai, Z. Lu, J. Yang, Citrate-based tannin-bridged bone composites for lumbar fusion. *Adv. Funct. Mater.* **30**, 2002438 (2020).
35. Z. Xie, Y. Zhang, L. Liu, H. Weng, R. P. Mason, L. Tang, K. T. Nguyen, J.-T. Hsieh, J. Yang, Development of intrinsically photoluminescent and photostable polylactones. *Adv. Mater.* **26**, 4491–4496 (2014).
36. J. Yang, Y. Zhang, S. Gautam, L. Liu, J. Dey, W. Chen, R. P. Mason, C. A. Serrano, K. A. Schug, L. Tang, Development of aliphatic biodegradable photoluminescent polymers. *Proc. Natl. Acad. Sci. U.S.A.* **106**, 10086–10091 (2009).
37. D. Shan, J.-T. Hsieh, X. Bai, J. Yang, Citrate-based fluorescent biomaterials. *Adv. Healthc. Mater.* **7**, 1800532 (2018).
38. Z. Xie, J. P. Kim, Q. Cai, Y. Zhang, J. Guo, R. S. Dhami, L. Li, B. Kong, Y. Su, K. A. Schug, J. Yang, Synthesis and characterization of citrate-based fluorescent small molecules and biodegradable polymers. *Acta Biomater.* **50**, 361–369 (2017).
39. P. Petrus, S. Lecoutre, L. Dollet, C. Wiel, A. Sulen, H. Gao, B. Tavira, J. Laurencikiene, O. Rooyackers, A. Checa, I. Douagi, C. E. Wheelock, P. Arner, M. McCarthy, M. O. Bergo, L. Edgar, R. P. Choudhury, M. Aouadi, A. Krook, M. Rydén, Glutamine links obesity to inflammation in human white adipose tissue. *Cell Metab.* **31**, 375–390.e11 (2020).
40. X. Chen, C. Zhang, F. Peng, L. Wu, D. Zhuo, L. Wang, M. Zhang, Z. Li, L. Tian, Y. Jie, Y. Huang, X. Yang, X. Li, F. Lei, Y. Cheng, Identification of glutamine as a potential therapeutic target in dry eye disease. *Signal Transduct. Target. Ther.* **10**, 27 (2025).
41. J. Li, H. Ke, X. Lei, J. Zhang, Z. Wen, Z. Xiao, H. Chen, J. Yao, X. Wang, Z. Wei, H. Zhang, W. Pan, Y. Shao, Y. Zhao, D. Xie, C. Zeng, Controlled-release hydrogel loaded with magnesium-based nanoflowers synergize immunomodulation and cartilage regeneration in tendon-bone healing. *Bioact. Mater.* **36**, 62–82 (2024).
42. Y. Wu, J. Du, Q. Wu, A. Zheng, L. Cao, X. Jiang, The osteogenesis of Ginsenoside Rb1 incorporated silk/micro-nano hydroxyapatite/sodium alginate composite scaffolds for calvarial defect. *Int. J. Oral Sci.* **14**, 10 (2022).
43. C.-S. Lee, S. Kim, J. Fan, H. S. Hwang, T. Aghaloo, M. Lee, Smoothened agonist sterosome immobilized hybrid scaffold for bone regeneration. *Sci. Adv.* **6**, eaaz7822 (2020).
44. Q. Gan, L. Chen, H.-P. Bei, S.-W. Ng, H. Guo, G. Liu, H. Pan, C. Liu, X. Zhao, Z. Zheng, Artificial cilia for soft and stable surface covalent immobilization of bone morphogenetic protein-2. *Bioact. Mater.* **24**, 551–562 (2023).
45. Z. Zheng, Y. Chen, H. Hong, Y. Shen, Y. Wang, J. Sun, X. Wang, The "yin and yang" of immunomodulatory magnesium-enriched graphene oxide nanoscrolls decorated biomimetic scaffolds in promoting bone regeneration. *Adv. Healthc. Mater.* **10**, 2000631 (2021).
46. Y. Zhu, H. Liang, X. Liu, J. Wu, C. Yang, T. M. Wong, K. Y. H. Kwan, K. M. C. Cheung, S. Wu, K. W. K. Yeung, Regulation of macrophage polarization through surface topography design to facilitate implant-to-bone osteointegration. *Sci. Adv.* **7**, eabf6654 (2021).
47. S. Li, H. Yang, X. Qu, Y. Qin, A. Liu, G. Bao, H. Huang, C. Sun, J. Dai, J. Tan, J. Shi, Y. Guan, W. Pan, X. Gu, B. Jia, P. Wen, X. Wang, Y. Zheng, Multiscale architecture design of 3D printed biodegradable Zn-based porous scaffolds for immunomodulatory osteogenesis. *Nat. Commun.* **15**, 3131 (2024).
48. P.-S. Liu, H. Wang, X. Li, T. Chao, T. Teav, S. Christen, G. Di Conza, W.-C. Cheng, C.-H. Chou, M. Vavakova, C. Muret, K. Debackere, M. Mazzone, H.-D. Huang, S.-M. Fendt, J. Ivanisevic, P.-C. Ho, α-ketoglutarate orchestrates macrophage activation through metabolic and epigenetic reprogramming. *Nat. Immunol.* **18**, 985–994 (2017).
49. M. Bessa-Gonçalves, C. Ribeiro-Machado, M. Costa, C. Ribeiro, J. Barbosa, M. Barbosa, S. Santos, Magnesium incorporation in fibrinogen scaffolds promotes macrophage polarization towards M2 phenotype. *Acta Biomater.* **155**, 667–683 (2023).
50. Y. Xiong, Z. Lin, P. Bu, T. Yu, Y. Endo, W. Zhou, Y. Sun, F. Cao, G. Dai, Y. Hu, L. Lu, L. Chen, P. Cheng, K. Zha, M. Shahbazi, Q. Feng, B. Mi, G. Liu, A whole-course-repair system based on neurogenesis-angiogenesis crosstalk and macrophage reprogramming promotes diabetic wound healing. *Adv. Mater.* **35**, 2212300 (2023).
51. D. Garcia, R. J. Shaw, AMPK: Mechanisms of cellular energy sensing and restoration of metabolic balance. *Mol. Cell* **66**, 789–800 (2017).
52. C.-T. Chen, Y.-R. V. Shih, T. K. Kuo, O. K. Lee, Y.-H. Wei, Coordinated changes of mitochondrial biogenesis and antioxidant enzymes during osteogenic differentiation of human mesenchymal stem cells. *Stem Cells* **26**, 960–968 (2008).
53. Z.-N. Ling, Y.-F. Jiang, J.-N. Ru, J.-H. Lu, B. Ding, J. Wu, Amino acid metabolism in health and disease. *Signal Transduct. Target. Ther.* **8**, 345 (2023).
54. L. Shen, Y. Yu, Y. Zhou, S. M. Pruett-Miller, G.-F. Zhang, C. M. Karner, SLC38A2 provides proline to fulfill unique synthetic demands arising during osteoblast differentiation and bone formation. *eLife* **11**, e76963 (2022).
55. Y. Yu, H. Newman, L. Shen, D. Sharma, G. Hu, A. J. Mirando, H. Zhang, E. Knudsen, G.-F. Zhang, M. J. Hilton, C. M. Karner, Glutamine metabolism regulates proliferation and lineage allocation in skeletal stem cells. *Cell Metab.* **29**, 966–978.e4 (2019).
56. D. Wang, J. Cai, Q. Pei, Z. Yan, F. Zhu, Z. Zhao, R. Liu, X. Guo, T. Sun, J. Liu, Y. Tian, H. Liu, X. Shao, J. Huang, X. Hao, Q. Chang, Z. Luo, D. Jing, Gut microbial alterations in arginine metabolism determine bone mechanical adaptation. *Cell Metab.* **36**, 1252–1268.e8 (2024).
57. J. Plummer, M. Park, F. Perodin, M. C. Horowitz, J. R. Hens, Methionine-restricted diet increases miRNAs that can target RUNX2 expression and alters bone structure in young mice. *J. Cell. Biochem.* **118**, 31–42 (2017).
58. S. Stegen, K. Moermans, I. Stockmans, B. Thienpont, G. Carmeliet, The serine synthesis pathway drives osteoclast differentiation through epigenetic regulation of NFATc1 expression. *Nat. Metab.* **6**, 141–152 (2024).
59. S. K. Wculek, G. Dunphy, I. Heras-Murillo, A. Mastrangelo, D. Sancho, Metabolism of tissue macrophages in homeostasis and pathology. *Cell. Mol. Immunol.* **19**, 384–408 (2022).
60. C. Jo, S. Park, S. Oh, J. Choi, E.-K. Kim, H.-D. Youn, E.-J. Cho, Histone acylation marks respond to metabolic perturbations and enable cellular adaptation. *Exp. Mol. Med.* **52**, 2005–2019 (2020).
61. A. J. Covarrubias, H. I. Aksoylar, J. Yu, N. W. Snyder, A. J. Worth, S. S. Iyer, J. Wang, I. Ben-Sahra, V. Byles, T. Polynne-Stapornkul, E. C. Espinosa, D. Lamming, B. D. Manning, Y. Zhang, I. A. Blair, T. Horng, Akt-mTORC1 signaling regulates Acly to integrate metabolic input to control of macrophage activation. *eLife* **5**, e11612 (2016).

62. Y. Li, Y.-C. Li, X.-T. Liu, L. Zhang, Y.-H. Chen, Q. Zhao, W. Gao, B. Liu, H. Yang, P. Li, Blockage of citrate export prevents TCA cycle fragmentation via Irg1 inactivation. *Cell Rep.* **38**, 110391 (2022).
63. J.-P. Auger, M. Zimmermann, M. Faas, U. Stifel, D. Chambers, B. Krishnacoumar, R. V. Taudte, C. Grund, G. Erdmann, C. Scholtysek, S. Uderhardt, O. Ben Brahim, M. Pascual Maté, C. Stoll, M. Böttcher, K. Palumbo-Zerr, M. S. J. Mangan, M. Dzamukova, M. Kieler, M. Hofmann, S. Blüml, G. Schabbauer, D. Mougiakakos, U. Sonnewald, F. Hartmann, D. Simon, A. Kleyer, A. Grüneboom, S. Finotto, E. Latz, J. Hofmann, G. Schett, J. Tuckermann, G. Krönke, Metabolic rewiring promotes anti-inflammatory effects of glucocorticoids. *Nature* **629**, 184–192 (2024).
64. W. Sun, B. Ye, S. Chen, L. Zeng, H. Lu, Y. Wan, Q. Gao, K. Chen, Y. Qu, B. Wu, X. Lv, X. Guo, Neuro–bone tissue engineering: emerging mechanisms, potential strategies, and current challenges. *Bone Res.* **11**, 65 (2023).
65. W. Xia, J. Xie, Z. Cai, X. Liu, J. Wen, Z.-K. Cui, R. Zhao, X. Zhou, J. Chen, X. Mao, Z. Gu, Z. Zou, Z. Zou, Y. Zhang, M. Zhao, M. Mac, Q. Song, X. Bai, Damaged brain accelerates bone healing by releasing small extracellular vesicles that target osteoprogenitors. *Nat. Commun.* **12**, 6043 (2021).
66. Z. Zhang, F. Wang, X. Huang, H. Sun, J. Xu, H. Qu, X. Yan, W. Shi, W. Teng, X. Jin, Z. Shao, Y. Zhang, S. Zhao, Y. Wu, Z. Ye, X. Yu, Engineered sensory nerve guides self-adaptive bone healing via NGF-TrkA signaling pathway. *Adv. Sci.* **10**, 2206155 (2023).
67. G. B. Kim, Y. Chen, W. Kang, J. Guo, R. Payne, H. Li, Q. Wei, J. Baker, C. Dong, S. Zhang, P. K. Wong, E. B. Rizk, J. Yan, J. Yang, The critical chemical and mechanical regulation of folic acid on neural engineering. *Biomaterials* **178**, 504–516 (2018).
68. Z. Wang, Z. Wang, W. W. Lu, W. Zhen, D. Yang, S. Peng, Novel biomaterial strategies for controlled growth factor delivery for biomedical applications. *npg Asia Mater.* **9**, –e435 (2017).
69. L. Qin, S. Yang, C. Zhao, J. Yang, F. Li, Z. Xu, Y. Yang, H. Zhou, K. Li, C. Xiong, W. Huang, N. Hu, X. Hu, Prospects and challenges for the application of tissue engineering technologies in the treatment of bone infections. *Bone Res.* **12**, 28 (2024).
70. M. Wu, Y. Zhao, M. Tao, M. Fu, Y. Wang, Q. Liu, Z. Lu, J. Guo, Malate-based biodegradable scaffolds activate cellular energetic metabolism for accelerated wound healing. *ACS Appl. Mater. Interfaces* **15**, 50836–50853 (2023).
71. X. Yu, H. Wu, J. Su, X. Liu, K. Liang, Q. Li, R. Yu, X. Shao, H. Wang, Y.-L. Wang, N. Shyh-Chang, Acetyl-CoA metabolism maintains histone acetylation for syncytialization of human placental trophoblast stem cells. *Cell Stem Cell* **31**, 1280–1297.e7 (2024).
72. A. Pouikli, S. Parekh, M. Maleszewska, C. Nikopoulou, M. Baghdadi, I. Tripodi, K. Folz-Donahue, Y. Hinze, A. Mesaros, D. Hoey, P. Giavalisco, R. Dowell, L. Partridge, P. Tessarz, Chromatin remodeling due to degradation of citrate carrier impairs osteogenesis of aged mesenchymal stem cells. *Nat. Aging* **1**, 810–825 (2021).
73. S. Bandyopadhyay, M. P. Duffy, K. J. Ahn, J. H. Sussman, M. Pang, D. Smith, G. Duncan, I. Zhang, J. Huang, Y. Lin, B. Xiong, T. Imtiaz, C.-H. Chen, A. Thadi, C. Chen, J. Xu, M. Reichart, Z. Martinez, C. Diorio, C. Chen, V. Pillai, O. Snaith, D. Oldridge, S. Bhattacharyya, I. Maillard, M. Carroll, C. Nelson, L. Qin, K. Tan, Mapping the cellular biogeography of human bone marrow niches using single-cell transcriptomics and proteomic imaging. *Cell* **187**, 3120–3140.e29 (2024).
74. Z. He, A. Brazovskaja, S. Ebert, J. G. Camp, B. Treutlein, CSS: Cluster similarity spectrum integration of single-cell genomics data. *Genome Biol.* **21**, 224 (2020).
75. K. Street, D. Risso, R. B. Fletcher, D. Das, J. Ngai, N. Yosef, E. Purdom, S. Dudoit, Slingshot: Cell lineage and pseudotime inference for single-cell transcriptomics. *BMC Genomics* **19**, 477 (2018).
76. D. Shan, S.-R. Kothapalli, D. J. Ravnic, E. Gerhard, J. P. Kim, J. Guo, C. Ma, J. Guo, L. Gui, L. Sun, D. Lu, J. Yang, Development of citrate-based dual-imaging enabled biodegradable electroactive polymers. *Adv. Funct. Mater.* **28**, 1801787 (2018).

Acknowledgments: We thank A. Ross and other staff at Center for Quantitative Imaging for μCT scanning. We thank M. Hazen at Microscopy Facility for assistance with fluorescence imaging. We thank J. Anderson at Materials Characterization Laboratory for assistance with SEM imaging. We thank A. Shay at Metabolomics Core Facility for assistance with sample running. We thank L. Liermann at Laboratory for Isotopes and Metals in the Environment for assistance with magnesium release analysis. All the facilities mentioned are from Penn State University. **Funding:** This work was supported by the National Key Research and Development Program of China 2024YFA1107800 (to J.Y.), the US Nationals Institutes of Health grant R01NS123433 (to S.Y.), the US Nationals Institutes of Health grant R01HL158204 (to S.Y.), and the Foundation of Muyuan Laboratory 13166022401 (to J.Y.). **Author contributions:** Conceptualization: J.Y., S.Y., H.X., and A.D.A. Methodology: S.Y., H.X., E.G., S.-R.K., J.Y., and E.B.R. Investigation: H.X., X.T., S.Y., E.G., E.B.R, R.R., and Y.W. Visualization: H.X., H.Z., E.G., and R.R. Supervision: J.Y., S.Y., S.-R.K., E.B.R., and A.D.A. Writing—original draft: H.X., S.Y., E.G., and H.Z. Writing—review and editing: H.X., S.Y., J.Y., E.G., and E.B.R. **Competing interests:** J.Y. and The Pennsylvania State University have a financial interest in Acuitive Technologies Inc. and Aleo BME Inc. A.D.A. has a financial interest in Zimmer Biomet and Aevumed. These interests are being managed by the respective institutions in accordance with established policies. H.X., E.G., S.Y., J.Y., and A.D.A. are listed as inventors on a patent application (PCT/US2025/029291) related to this study, which was filed by The Pennsylvania State University on 14 May 2025. The patent status is currently pending. All other authors declare that they have no competing interests. **Data and materials availability:** All data are available in the main text, the Supplementary Materials, and the auxiliary files section, except the scRNA-seq data of non-hematopoietic cells of hBM, which were downloaded from NCBI GEO (GSE253355).

Submitted 16 April 2025
Accepted 23 June 2025
Published 23 July 2025
10.1126/sciadv.ady2862